AAAS
Advanced Devices & Instrumentation
Volume 2022, Article ID 9861078, 24 pages
https://doi.org/10.34133/2022/9861078

Advanced Devices & Instrumentation
A SCIENCE PARTNER JOURNAL

Review Article

The Dawn of Metadevices: From Contemporary Designs to Exotic Applications

Sumbel Ijaz,[1] Ahsan Sarwar Rana,[2] Zubair Ahmad,[3] Muhammad Zubair,[1] Yehia Massoud,[4] and Muhammad Qasim Mehmood[1]

[1]*MicroNano Lab, Electrical Engineering Department, Information Technology University (ITU) of the Punjab, Ferozepur Road, Lahore 54600, Pakistan*
[2]*Department of Electrical & Computer Engineering, Air University, Islamabad, Pakistan*
[3]*Qatar University Young Scientists Center (QUYSC), Qatar University, 2713 Doha, Qatar*
[4]*Innovative Technologies Laboratories (ITL), King Abdullah University of Science and Technology (KAUST), Thuwal 23955-6900, Saudi Arabia*

Correspondence should be addressed to Muhammad Zubair; muhammad.zubair@itu.edu.pk, Yehia Massoud; yehia.massoud@kaust.edu.sa, and Muhammad Qasim Mehmood; qasim.mehmood@itu.edu.pk

Received 21 November 2021; Accepted 30 March 2022; Published 3 July 2022

In recent years, metamaterials and metasurfaces have prospered in many fields of "science and technology," covering the entire electromagnetic spectrum. Metasurface devices constituting of a set arrangement of meta-atoms translate into modern-day miniaturized means to achieve planar, ultrathin, multifunctional electromagnetic (EM) systems. Metasurfaces are ideal candidates to develop next-generation, lightweight, and fabrication-friendly optical components as they impart local and space-variant phase changes on incident EM waves, providing more comprehensive control over EM wavefronts. This attribute has been instrumental in realizing a variety of special beams for high-capacity data transmission and superresolution imaging. Furthermore, from the perspective of efficiency, the below-par performance of previously explored plasmonic-based metasurfaces can be enhanced by employing all-dielectric metasurfaces. All-dielectric metasurfaces with high refractive indices have high resonance quality factors, low cost, and CMOS fabrication compatibility. 2D materials-based metasurface design has succeeded in further reducing the device footprints for better integration in optoelectronic devices. The conventional, time- and computation-intensive EM solvers have largely been assisted by artificial intelligence techniques, resulting in quicker metasurface designing. This review focuses on the state-of-the-art meta-devices employed for wavefront manipulations of optical waves. The design variants and applications of metasurfaces constitute a prolific field for future research to meet existing challenges and make the devices more suitable for real-time applications.

1. Introduction

A range of electromagnetic (EM) radiations spanning from radiofrequency to gamma rays (greater than about 10^{19} cycles per second), and many intermediate frequency regimes set up the EM spectrum. The radio, microwave, and infrared have wide-ranging applications in telecommunication, precisely for audio/video transmission and reception, broadcasting and navigation, satellite communication, radar signals, wireless communication systems, and thermal heating. However, the higher-frequency EM waves including ultraviolet, X-rays, and gamma rays are ideal for high-resolution bioimaging, sterilization, and radiotherapy. Optical spectrum extending from 400 THz to 750 THz is particularly suitable for lensing, holography, lasers, and optical communication since it has a major advantage of lying in the visible spectrum of EM waves (waves that can be detected with the help of our eyes) [1].

Mathematically, the time-varying electromagnetic (EM) wave propagating in free space follows the model given below [2]:

$$E(\boldsymbol{r},t) = \hat{a}\, E_0(x,y,t)|E(x,t)|e^{k_0 kz} e^{-jk_0 nz} e^{j\omega t} \quad (1)$$

(Polarization vector; Temporal variable; Spatial variables; Amplitude; Phase; Frequency)

where $\hat{a}$ is the polarization vector, t is time, n and k represent real and imaginary parts of optical constant, and $E_0(x,y,t)$ represents spatial structure; $E(x,y,t)e^{k_0 kz}$, $e^{-jk_0 nz}$, and $e^{j\omega t}$ provide the amplitude, phase, and frequency information, respectively, while ω stands for angular frequency. An in-depth examination of the expression leads to finding out the degrees of freedom of the EM wave elaborated in Figure 1(a), which are engineered for desired applications at nanoscale [3].

Only some of the EM wave characteristics undergo a variation when it propagates through a natural material as the size of the atoms is too small in comparison with its wavelength to make any significant changes. On the contrary, one can establish full control over EM wave's properties such that they exhibit unconventional functionalities by modifying the spatial profile of the optical phase, as desired. This feature is almost impossible to realize using naturally present materials. However, by using 2D or 3D arrays of artificially engineered subwavelength nanoresonators known as "meta-atoms," the phase of EM wave can be tailored as per requirement. When meta-atoms are arranged in 3D space with considerable thickness, they constitute a "metamaterial" whereas if their thickness is of subwavelength scale that arrangement is termed as "metasurface." To state it another way, metasurfaces are described as an arrangement of constant amplitude dipoles with engineered phase profiles. This implies that the overall intensity of the field emitted from the metasurface is a superposition from many dipole antennas. Artificial EM metamaterials yield unconventional physical properties (as compared to naturally occurring materials), such as the negative dielectric constant, negative permeability, nonlinear effects, enhanced or suppressed backscattering, tunability, reconfigurability, enhanced plasmonic effects, engineered dielectric resonances, and strong chiral properties [4–6]. As a material is characterized by its electric and magnetic properties, therefore, the design of a metamaterial involves engineering of its electric permittivity (epsilon 'ε') and magnetic permeability (mu 'μ') as was indicated in 1968 [7]. The parameters epsilon and mu are significant while considering a material and its interaction with an EM wave, since they determine the refractive index of a material, which, in turn, dictates the propagation, radiation, or scattering of the EM wave. The refractive index has real and imaginary components as 'n' and 'k,' which are related by Kramers–Kronig integral [8], and the complex refractive index is given by $\mathbb{N} = n + jk$, determining whether the material would be a dielectric with $n > 0$ or a passive one with $k > 0$. The refractive index depends on the constitutive parameters as $\mathbb{N}(\omega) = \sqrt{\mu(\omega)\varepsilon(\omega)}$.

1.1. Design of Metasurfaces. On a microscopic level, metamaterials can be deemed as artificially engineered heterogeneous entities that are designed by using natural materials in the form of special periodic/aperiodic arrangements. These arrangements employ fundamental building blocks known as meta-atoms or unit cells for the design. These meta-atoms tailor properties of the metamaterial in response to electromagnetic waves. Furthermore, these meta-atoms can also be found in the form of isotropic/anisotropic, single or supercell arrangements in a metasurface, as can be seen from Figures 1(b)–1(e). Since these periodic atoms employ natural materials in their design, the same cell configuration provides a multifaceted control of phase fronts. The electromagnetic multipoles stimulated inside meta-atoms behaving as scatterers [9] provide independent phase (and amplitude) manipulation capability at element level by engineering their geometry, such that EM wavefronts are precisely modified [10] for optoelectronic applications. An appropriate selection of spatial distribution, geometry, and orientation of subwavelength resonators and the material to be employed is essential to realize desired functionalities.

In terms of geometry, there are two fundamental profiles assumed by meta-atoms: rectangular and cylindrical. A meta-atom of rectangular nanobar shape introduces a phase shift of π radians so that the state of polarization is switched from one to another effectively, thus acting as a half-wave plate (HWP). The HWPs can also be realized by combining two quarter-waveplates (QWPs), which introduce a phase shift of $\pi/2$ to the light beam passing through them. The cylindrical nanopillars are essentially the step-index waveguides as they have the field localized within them because of the difference of their refractive index with the surrounding air. The phase coverage in this case is achieved by varying the diameter obeying step-index waveguide theory [11, 12]. However, when meta-atoms are arranged so as to combine multiple anisotropic nanoantennas (HWPs), they form a supercell [13, 14] which helps exploiting functions that are not realized using single nanoresonators because of the provision of additional degrees of freedom [15]. A supercell can be realized by arranging them laterally with equal or unequal dimensions. A design of four unit cells making a supercell is presented in [16] to induce chirality for high broadband asymmetric transmission for LCP incidence, whereas the one in Figure 1(e) is a hybrid, polarization-insensitive supercell, where both Pancharatnam-Berry (PB) and propagation phases are used to achieve full control of the phase of incident light of any polarization. Such a supercell has been shown to achieve circular- and giant spin-selective-asymmetric transmission [17].

Alongside geometry or shape of the meta-atom, the geometrical dimensions, i.e., lattice constant and lateral extent (length for rectangular profiles and diameter for cylindrical ones), pose optimization challenges in order to make the design feasible for fabrication. For example, the diameter of nanopillars cannot be decreased beyond a certain height-to-

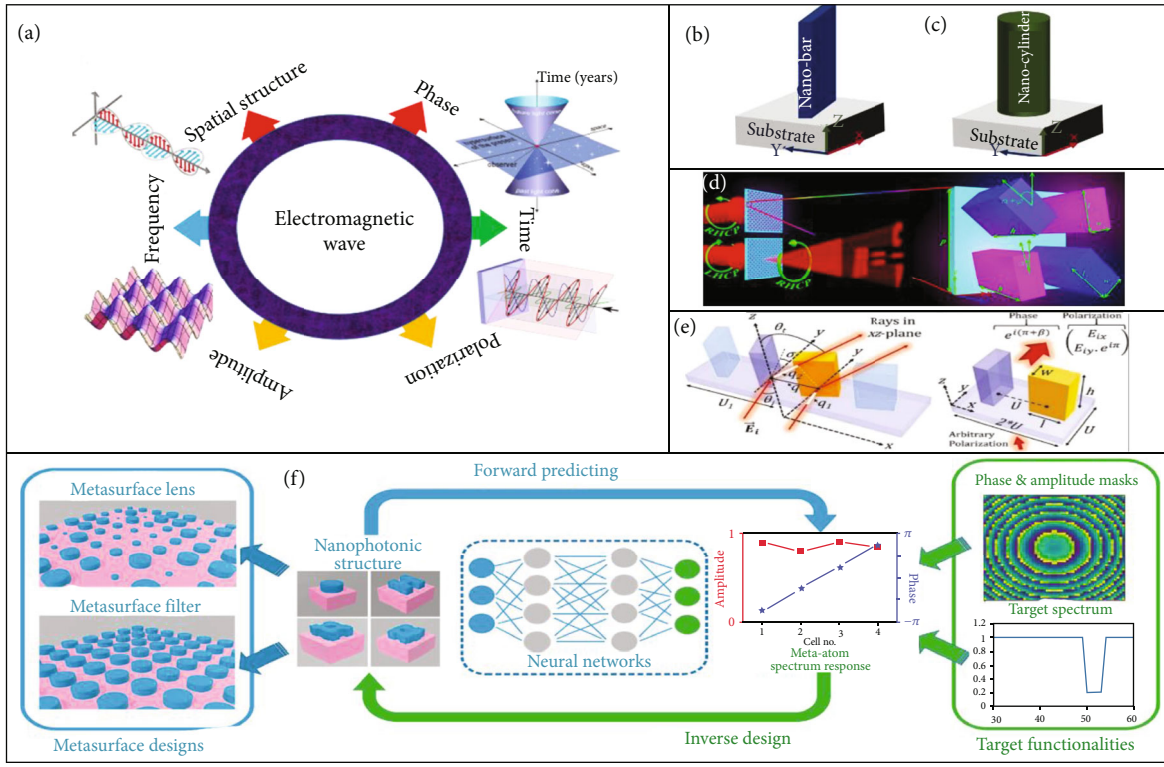

FIGURE 1: Metasurfaces—capabilities and design. (a) Electromagnetic wave and the degrees of freedom to be engineered. (b) Unit cell/meta-atom/nanoresonator/nanoantenna/HWP. (c) Unit cell of step-indexed, cylindrical, nanowaveguide on a dielectric base. (d) A supercell with x-y symmetry (reprinted with permission from [16], copyright 2020 American Chemical Society). (e) A supercell with rectangular base: a combination of HWPs to achieve broadband polarization-insensitive phase control (source: Ansari et al. [15]; copyright 2020 licensed under Copyright Clearance Center, Inc.). (f) Deep learning-based, forward and inverse metalens and metasurface filter designs with various meta-atom/nanophotonic structures for predicting the EM response and geometry from the spectrum based on both amplitude and phase responses. The depicted predicting neural network (PNN) (reprinted with permission from [48]; copyright © 2019 American Chemical Society)

diameter ratio (aspect ratio). Similarly, a nanopillar cannot assume a diameter greater than the period of the unit cell itself, as constrained by the Nyquist criterion for fabrication of meta-atoms (period $< (\lambda/(2\text{NA}))$). Following such precautions during design and fabrication is the key to ensuring full-phase coverage of 2π with the variation of diameter within allowable limits [11].

Metasurfaces can be classified according to the range of their operating frequencies such as microwave, terahertz, and optical [18] as they adopt sizes less than the operating frequency (they should have smaller dimensions than the corresponding operating wavelength). Another distinction in metasurface design can be made on the basis of their scattering properties, e.g., a metasurface can be reflective, transmissive, or absorptive [19]. They can also be categorized considering the type of material they are made of, e.g., metallic/plasmonic [20], high-index dielectric [21], a combination of metal, and dielectric or a 2D material-based metasurface [22].

For metal-based metasurfaces, plasmonic resonances resulting from the dynamic response of material's electrons to the external electromagnetic field lead to strong light-matter interactions. Earlier, various transmission and reflection type subwavelength scatterer's metasurfaces were demonstrated based on noble metals including gold [23] and silver [24]. Atypical refractions were observed, which were either due to light scattered from the metallic antennas [25] or due to excitation of a particular mode originating from nanosieves and subwavelength waveguides. Plasmonic metasurfaces pose fabrication challenges and get contaminated when immersed in liquids [26]. There exist ohmic losses in metals due to strong electron-electron and electron-phonon scattering, which limit the performance of metal-based plasmonic metasurfaces in the visible regime due to absorption. The energy of the impinged light is transformed to thermal energy in the material, thus making plasmonic-based metasurfaces less attractive for high-efficiency applications [27]. The devices' efficiency is even worsened when fabrication defects are factored in [28].

To attain high efficiency by mitigating nonradiative losses, all-dielectric metasurfaces have emerged as a promising alternative to plasmonics [29]. All-dielectric metasurfaces exhibit both magnetic and electric dipoles leading to the creation of antiferromagnetic resonances [30] and higher-order Mie resonances. Higher-order Mie resonances refer to the generation of quadrupole and octupole configurations, along with electromagnetic dipole, for materials having $\varepsilon > 0$, which leads to superior performance than

plasmonics-based structures [31]. This design of metasurfaces takes advantage of the low extinction coefficient at optical frequencies to attain maximum transmission by minimizing absorption loss [32]. Metasurfaces based on silicon (Si)—one of the earliest known dielectrics—have extensively been designed because of the associated advantages of low cost and ease of fabrication. However, the performance of Si-based metasurfaces is better for infrared regime because of its 1.12 eV bandgap, while amorphous silicon (a-Si), because of having 1.7 eV bandgap, performs well for (near-infrared-visible frequencies) [33]. An a-Si-based metasurface is reported in [34], achieving broadband operation and exhibiting an efficiency as high as 75% in the 1000-1400 nm range.

Other dielectric materials such as titanium oxide (TiO_2) [27] and gallium nitride (GaN) [35] have also been explored for metasurfaces. These dielectrics acquire ultrahigh transmission efficiency for lensing and holography in visible regime. As an example in point, authors in [33] have demonstrated a high-performance metahologram for RGB wavelengths with >78% efficiency. However, the designs from these dielectrics require high aspect ratios (up to 10 or 15), to attain the desired phase making them infeasible for fabrication [35]. For this reason, novel dielectric materials with high refractive indices and low extinction coefficients such as gallium phosphide (GaP) and hydrogenated amorphous silicon (a-Si:H) have been sought for use in visible regime. The addition of hydrogen in a-Si increases its mobility bandgap and decreases the extinction coefficient. Moreover, a-Si:H has added benefits of being a low-cost, highly efficient, and nanophotonic complementary metal-oxide-semiconductor- (CMOS-)- compatible material, thus making it an ideal candidate for designing devices requiring minimal loss for the optical regime.

In instances where asymmetric transmission plays a pivotal role in achieving targeted functionalities, such as those in quantum physics where controlling electrons' spin momentum (polarization of the wave) is critical [36, 37], it is instrumental to be able to design a multifunctional metasurface where both phase and polarization state act as degrees of freedom. In [21], a monolayer all-dielectric metasurface is reported where asymmetric transmission of CP light is realized by wavefront engineering. The structural analysis of the transmission phenomenon has been carried out using the Jones calculus, where it attains a 76% asymmetric transmission parameter. So far, such a transmission [38] has mostly been possible for microwave or infrared domains. However, such structures have been employed to produce metaholograms for visible regime as well [30, 39].

The phase manipulation has helped to miniaturize devices to attain multiple functionalities, which are exceedingly needed in integrated optical systems. The versatile applications in the optical regime include flat optical elements [40], retroreflectors for visible backscattering communication [41], modulators, aberration-corrected flat metalenses [35], waveplates, mirrors, super imaging [42], polarization converters, polarimeters [43], optical vortex generators [44, 45], beam splitters, filters employing structural color to visualize detailed colors beyond sRGB [46], multiplexed metahologram devices for 3D projective displays, invisibility cloaking [47], and anticounterfeiting technologies [21–23].

1.2. Role of Modeling and Simulation. Traditionally, the design and optimization of metasurfaces are executed using time-intensive and well-established computational electromagnetic methods, including but not limited to finite element methods, finite difference time domain (FDTD) method, method of moments, and transmission line matrix methods. These methods rely on iterative calculations performed to zero in on the most efficient set of design parameters for the metasurface under consideration. The advent of high-speed computers popularized the use of computing software for this purpose, which, while using the same techniques as before, helped reduce the computational time and labor involved to a great extent. Using commercial software packages like Lumerical FDTD, computer simulation technology (CST-MWS), and Comsol Multiphysics, simulations are carried out for computing the target electromagnetic (EM) responses. However, they expend a drastic computational effort in selection of meta-atom design as literally hundreds of EM simulations are run to solve Maxwell equations on a case-by-case basis.

More recently, deep learning methods have gained attention in this domain primarily due to their ability to make the design optimization process faster. These methods mimic the way humans gain certain types of knowledge, have risen to the forefront in many fields of research where there is a significant amount of data to be processed, and make the overall process quicker, more accurate and bias-free. The greater accuracy associated with these methods stems from making a holistic analysis by including all possible variables into the design process. Additionally, while humans tend to lean towards certain outcomes for a particular design problem, a deep-learning routine is virtually free of any such tendencies and thus yields bias-free results. A neural network is used in [48] that is capable of predicting phase and characterizing 3D dielectric structures, thus making their design easier and faster (Figure 1(f)). In [49], a complex, all-dielectric metasurface is modeled using the information of its geometry and governing physical principles as the network's input. The presented design is highly accurate as it achieves a very low average mean square error (MSE) (1.16×10^{-3}) and is quicker than traditional simulation methods.

A hybrid architecture of convolutional neural network (CNN) and recurrent neural network (RNN) is employed in [50] to predict the optical response of a metasurface absorber and emitter with all important dimensional parameters and their shapes as inputs. The hybrid, 98% faster model results in an MSE for test datasets as 7.3×10^{-4} and 6.2×10^{-4} for absorber and emitter cases, respectively. Similarly, a design-independent generative adversarial network (GAN) has been applied in [51] to speed up the metasurface design process. The network is also capable of suggesting different possible metasurface designs for a bifocal metalens and a polarization-independent metalens.

The field of nanophotonics offers various sophisticated methods and technologies for fabricating and integrating these metasurfaces [40]. These technologies include electron-beam lithography (EBL) [52], focused-ion beam (FIB) lithography [53], interference lithography, nanoimprint lithography [54], and femtosecond laser writing [55].

1.3. Working Principle of Metasurfaces. Unlike conventional optical elements that make use of phase accumulation for manipulating wavefronts, metasurfaces achieve this target in terms of phase, amplitude, and polarization using arrays of subwavelength optical resonators. EM waves can be modulated in terms of amplitude originating from ohmic losses and absorptive dissipation inherent to metals or plasmonic materials, in order to exploit absorption-based applications. For transmissive applications, phase-based metasurfaces are employed, which can be further divided into two types—a resonance type (design-dependent) involving propagation phase and geometrical type (usually associated with anisotropic structure) involving PB phase [56]. The complete range of phase accumulation is a function of material, spatial distribution of nanoresonators, geometry, and orientation with reference to a nearby nanoantenna. PB phase metasurfaces are capable of showing greater transmission over a wide range of wavelengths, while their utilization is limited to circularly polarized incident light. For such a design, every HWP produces a phase shift of $\pm 2\theta(\mathrm{x}, \mathrm{y})$, where θ represents the angle at which the meta-atom is oriented, and the handedness of incident light dictates the sign. Upon incidence of light, the nanoresonators introduce an abrupt phase change in the optical path along the interface between two media [4] and mold the incident wave in the desired direction. The metasurface imparts local and space-variant phase change on incident EM wave and provides a planar opportunity for controlling amplitude, polarization [57], and phase of EM wavefronts such that it offers great potential for developing new optical components. It is also worth mentioning that phase-modulating metasurfaces that follow resonance-dependent mechanisms exhibit lower conversion efficiency (ratio between the power of cross-polarized light and that of incident light $\eta_c = P_{\mp}/(P_{\mp}+P_{--}) \times 100\%$). In contrast, geometric metasurfaces rank higher when it comes to phase control by virtue of the spatially varying arrangements of nanoresonators [58, 59].

One of the more noteworthy contributions in this context was made by the Capasso group, when they proposed a V-shaped structure with different arm lengths and opening angles for subwavelength thick structures to introduce rapid phase changes for incoming light for wavelength manipulation [57]. Over the years, variously shaped plasmonic meta-atoms including nanogrooves, nanoslits, nanoholes, and split-ring resonators have also been explored to realize resonance metasurfaces. Phase gradient metasurfaces find applications in beam-steering, imaging, and holography [60].

In this review article, we will be presenting an overview of the metamaterials and metasurface-based devices that manipulate EM waves in the visible regime. The applications including absorption, metalensing, metaholography, polarization control, and the generation of different beams including airy, Bessel, and OAM will be discussed. Some other phenomena including reflection, chirality, sensing for refractive index, bioimaging, and biosensing will also be covered briefly.

2. Absorption

Absorbers are the devices that transform electromagnetic waves into heat energy by absorbing them. Absorption was observed as an indirect phenomenon in 1902 by Wood, when anomalous reflection dips from the metallic gratings were observed [61]. The absorptance is measured in terms of transmission and reflection of a material by using the relation stated in [62]

$$A = 1 - |\gamma| - |T|, \tag{2}$$

where t is transmission and Γ is reflection.

2.1. Metasurface/Metamaterial Absorbers. In the past, numerous plasmonic metamaterial and metasurface absorbers exhibiting plasmonic resonance have been profiled. But the scarcity of their reserves and high cost, poor thermal stability and inertness, uneconomical fabrication and pervasive nature hinder their use in applications involving solar thermophotovoltaics (STPVs), thermal emission, and hot electron generation. Aluminum (Al), which is both abundant and low cost, has also exhibited perfect absorption [49, 50]. However, its low melting point (660°C) and high chemical reactivity restrict its utilization for high-temperature applications [63]. Nickel (Ni) [64], chromium (Cr) [65], titanium (Ti) [66], tungsten (W) [62], molybdenum (Mo), and tantalum (Ta) [13], as well as refractory materials like titanium nitride (TiN) [67] and zirconium nitride (ZrN) [68], have all been investigated for the design of both absorbers and emitters. Emitters essentially exhibit narrowband absorption response and are augmented with broadband absorbers in solar thermal photovoltaic (STPV) applications. High-index dielectrics including Si, TiO_2 and Ge have also been reported for high absorptive performance [11, 69]. Multiband light absorption has been achieved by employing plasmonic-dielectric nanoantennas hybrid system or the all-dielectric metamaterials [63]. Nevertheless, dielectric absorbers have limited bandwidth and thus cannot be used in high-power applications because of low thermal stability. Refractory materials have shown significant promise as absorber materials owing to their plasmonic behavior in optical regime coupled with higher thermal stabilities. They have excellent absorption and are CMOS-compatible, corrosion- and high-temperature-resistant, mechanically strong, and durable.

It is of primary interest to reduce the dimensions of graded structures/Fabry-Perot-type cavity-based absorber designs using metamaterials and metasurfaces to facilitate their integration with compact optoelectronic systems. But many of the designs require patterning on subwavelength scales amounting to complex fabrication processes. Multiple pairs of stacked metal/dielectric resonators are used

frequently in the design of broadband absorbers because of the strong cavity resonance inside the film of dielectric material [70]. Moreover, the authors in [71] claim that an assembly of resonators assuming different shapes in one period has the potential to exhibit resonance at different wavelengths simultaneously.

An awaited revolution in the absorber design was seen when Landy et al. proposed metal-dielectric-metal (MDM) triple-layer metamaterials as perfect EM wave absorbers in 2008 [72]. Since then, various absorbers that assume the very topology for radiofrequency (RF), terahertz (THz) [73], mid-infrared (MIR) [74], near-infrared (NIR) [75], and visible frequencies [40, 41] have been designed with wider angular tolerance. Different types of EM resonances are to be credited for higher absorption of the incident light, such as Mie resonance [76], propagating surface plasmon resonance (PSPR) [77], localized surface plasmon resonance (LSPR) [78], and surface lattice resonance (SLR) [79], each of which can be single or multiple narrowband resonances.

Another characterization of absorber structure can be done from a macroscopic electromagnetic point of view, whereby the material's effective parameters "ε" and "μ" dictate its impedance (z) [4], given as $z = \sqrt{\mu/\varepsilon}$ [80]. The reflection becomes negligible for the wavelength at which the impedance is equal to that of free-space impedance while the transmission is already blocked by the ground plane, resulting in perfect absorption of incident waves because impedance is related to reflection and transmission as defined in [73]

$$z(\lambda) = \sqrt{\frac{(1 + R(\lambda))^2 + T(\lambda)^2}{(1 - R(\lambda))^2 - T(\lambda)^2}}. \tag{3}$$

With a view to investigate the relationship between structure geometry and achieve maximum absorption, a wide variety of structures, such as nanopillars [81], disks [82], nanopyramids [83], nanocones [84], nanoring grooved arrays [85], square rods [67], spheres, or randomly spread nanoparticles [86], have been explored. However, each of them poses a different set of design challenges, with the quest for an optimum configuration still underway.

Optical absorbers are employed in a wide arena of applications across the EM spectrum, such as photodetectors, photochemical and photovoltaic cells, optical filters, thermal imaging, stealth technology, thermal camouflaging and thermal light sources. On the other hand, wavelength-selective absorption finds applications in color filtering with enhanced color purity [87]. All-dielectric [88] design configurations, as well as MDMs [89], have the potential for behaving as color filters.

Many efficient and broadband solar absorbers of different shapes that fully capture incident sunlight [90] have so far been proposed. In [62], a tungsten-based absorber with square- and cross-shaped designs having a total thickness of 250 nm is presented with near-unity absorption for the entire visible range (Figure 2(a)). In [68], a ZrN-based ultrabroadband absorber is presented for energy harvesting using STPV systems with an average absorption of >95% for 400-800 nm and 86% for 280-2200 nm (Figure 2(b)). In [65], a 250 nm thick chromium-based circular ring-shaped absorber is presented, both numerically and experimentally having $A_{\text{sim}} > 98\%$ for 500-710 nm and A_{fab} of 96.5% for 500-800 nm (Figure 2(c)). All of these structures are polarization- and angle-insensitive. A TiN-based wide-angle ultrabroadband absorber exhibiting a strong absorption of 87% for 250-2300 nm with ultrathin thickness (330 nm) is presented in [91] (Figures 2(d)–2(f)). The outstanding performance of this absorber is realized with the help of resonant modes while emittance of 29% is in the wavelength range of 5000-13000 nm. In [92], an optimized pair of tungsten-based absorber and emitter for an STPV system is analyzed (Figures 2(g) and 2(h)). Similarly, a tantalum-made cross-shaped absorber-emitter pair is shown in Figures 2(i) and 2(j), where the emitter is so sharply narrowband that it matches the bandgap (0.55 eV) of an indium-gallium-arsenide-antimonide (InGaAsSb) PV cell [13]. The overall STPV efficiency has been reported as 41.8%.

3. Light Structuring (Metalensing, Holography, and OAM Generation)

Refraction of light in conventional optics obeys Snell's law; however, for heterogeneous materials or metamaterials where there is an abrupt phase discontinuity at the interface, the light beam redirection is not only determined by a sudden change of refractive indices but also by the distribution of phase discontinuities [93]. Generalized laws of refraction and reflection are demonstrated with the help of Figures 3(a) and 3(b), where it is evident that the interface leads to a noncoplanar anomalous beam generation, whose direction is dependent on the angle between the incident plane and antenna array. Abrupt phase discontinuity provides new degrees of freedom. V-shaped antennas have been deployed as phase elements with different opening angles, orientations and arm-lengths to modulate phase over a range of 2π radians [25]. C-shaped split-ring resonators [94], U-shaped split-ring resonators [95], and cross-shaped resonators [96] have also been explored to achieve phase discontinuities. The light reflection and refraction at the interface with a phase gradient is given by [97]

$$\cos\vartheta_r \sin\varphi_r = \frac{1}{n_i k_0}\frac{d\varnothing}{dx}, \tag{4a}$$

$$n_i \sin\vartheta_r - n_i \sin\vartheta_i = \frac{1}{k_0}\frac{d\varnothing}{dy}, \tag{4b}$$

$$\cos\vartheta_t \sin\varphi_t = \frac{1}{n_t k_0}\frac{d\varnothing}{dx}, \tag{5a}$$

$$n_t \sin\vartheta_t - n_i \sin\vartheta_i = \frac{1}{k_0}\frac{d\varnothing}{dy}. \tag{5b}$$

Here, ϑ represents the angle between propagation vector and its projection on the xz-plane whereas φ represents the projection angle of the wave vector on the xz-plane and z-axis.

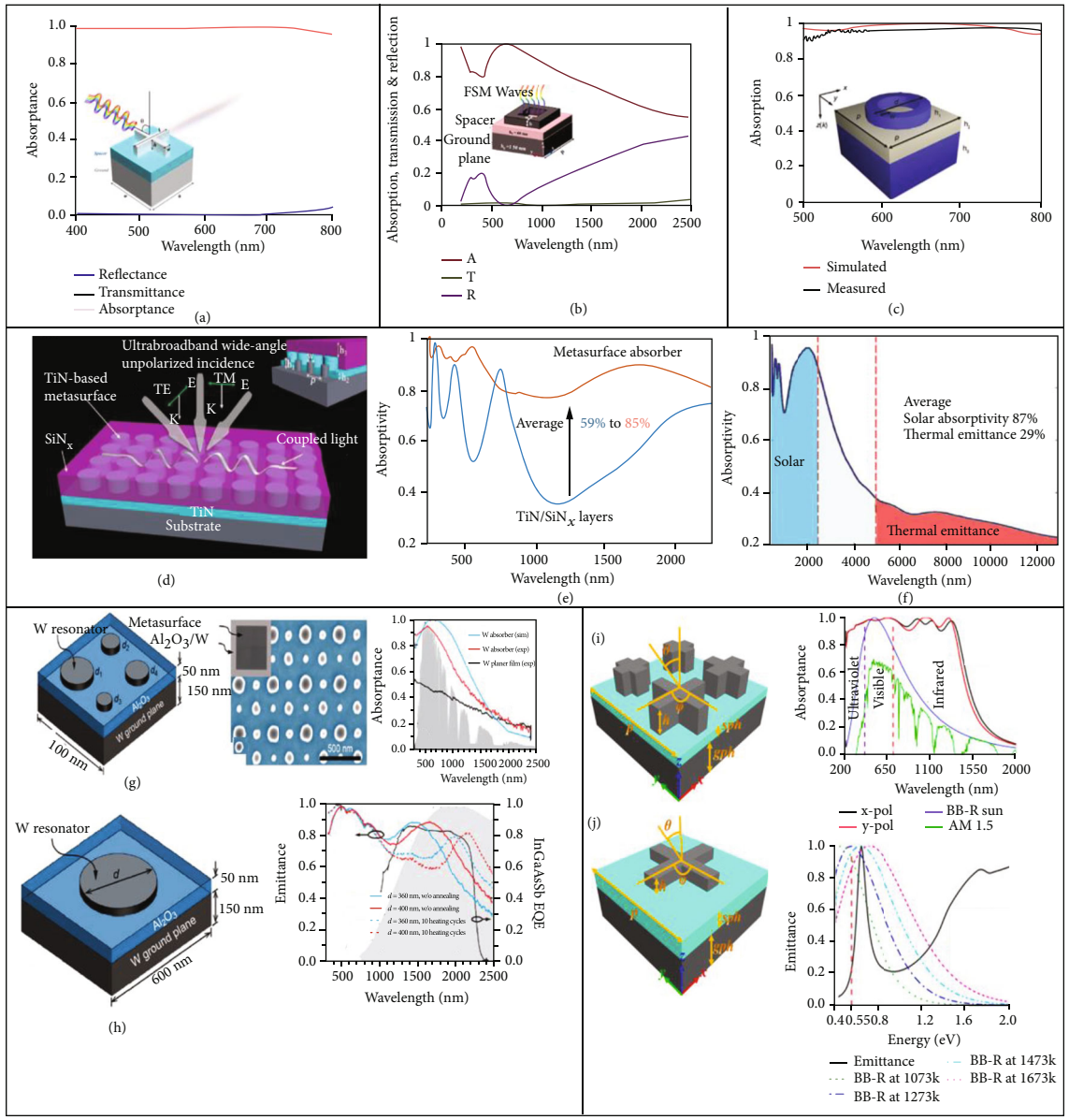

FIGURE 2: Absorber designs and their performance. (a) Tungsten-based, cross-shaped, ultrathin absorber. Source: Rana et al. [62] (licensed under the terms of the Creative Commons CC). (b) Zirconium nitride-based square ring-shaped broadband absorber (reprinted with permission from [68] © The Optical Society). (c) Chromium-based circular ring-shaped thermally robust absorber (source: Kim et al. [65], licensed under the terms of the Creative Commons CC). (d–f) TiN-based metasurface absorber with SiO_2-TiN cylinder arrays embedded inside the SiN_x; measured absorption with and without grating and calculated absorption of the metasurface absorber for an ultrabroadband region [91] (copyright Wiley-VCH GmbH. Reproduced with permission). (g, h) Tungsten (W) metasurface solar absorber and emitter. (g) Supercell consisting of four nanodisks with sapphire spacer and tungsten ground plane; SEM image of the fabricated absorber and measured (red) and simulated (cyan) absorptances. (h) Tungsten-based nanodisk emitter, sapphire spacer, and tungsten ground plane, along with obtained emittance (reprinted with permission from [92]. copyright 2018 American Chemical Society). (i, j) Tantalum metasurface solar absorber and emitter. (i) Supercell consisting of four cross-structures and the absorptance curve. (j) Cross-shaped emitter unit cell with emittance plot and blackbody radiation curves at 1073 K, 1273 K, 1473 K, and 1673 K (source: Sarwar et al. [13] © 2021, licensed under the Creative Common).

Traditional optics—lenses, waveplates, filters, and the like—have existed for centuries and despite refinements; they have not largely been changed requiring machining and angling of the glass for realization of the desired operation. Lenses find applications in various fields of science including medicine, biology, optics, photonics, and security [40]. They are employed in imaging, spectroscopy, endoscopy, full-color routing, robotic vision, and self-driving vehicles. The conventional lenses are bulky and unfit for being used in a compact system. More recently, metasurface optics has emerged offering compactness and a new range of functionalities not accessible with bulk optical elements. High-

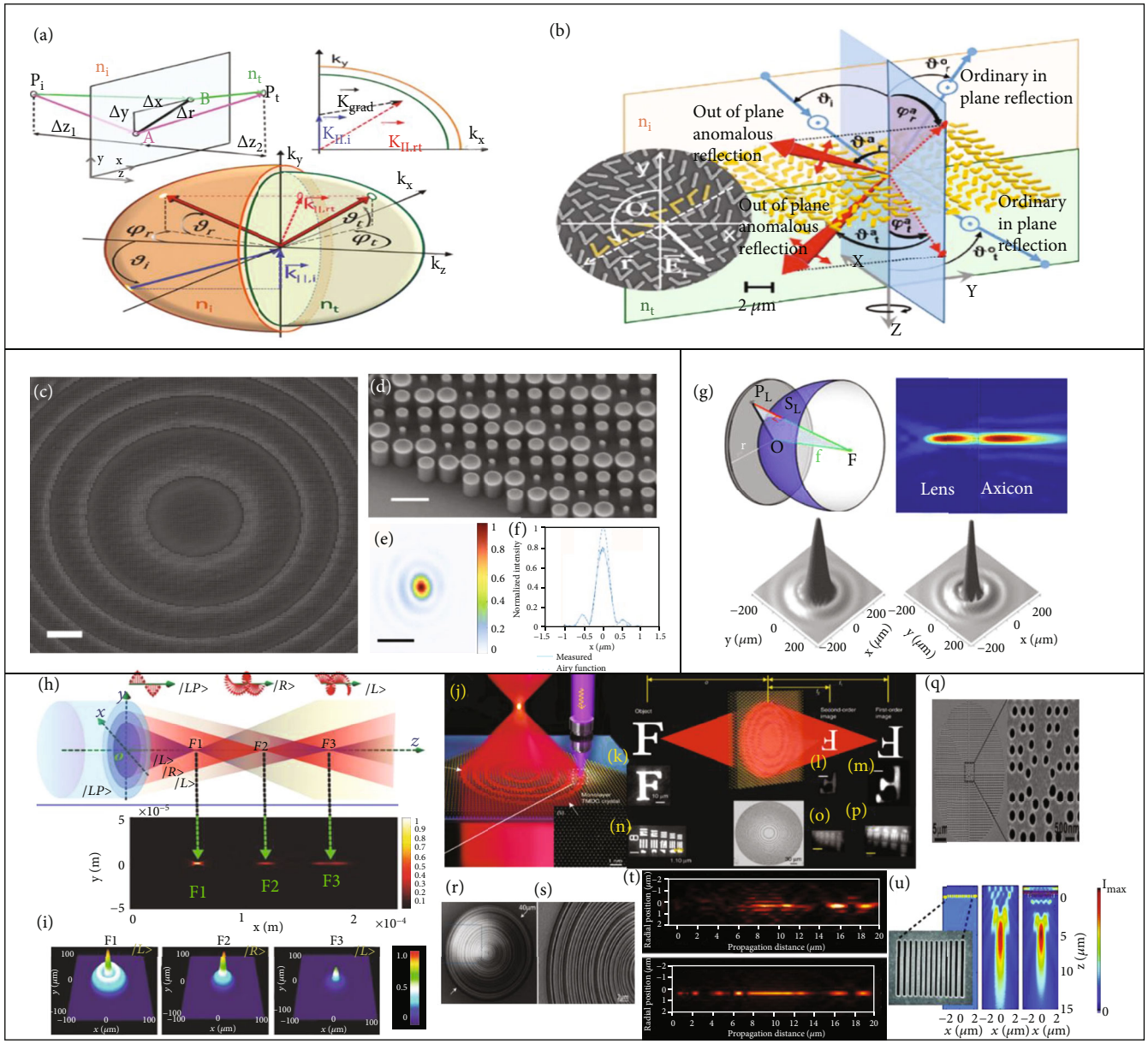

FIGURE 3: Light structuring through phase manipulation. (a) Illustration of generalized laws of reflection and refraction of light for interface between two media "n_i" and "n_t." (b) Incidence of light (θ_i w.r.t z-axis on the interface, i.e., xy-plane); Incidence of light on a periodically translated eight V-shaped subwavelength antennas depicting co- and cross-polarized components of reflected ϑ_r^o and refracted light ϑ_t^o. The anomalous modes are determined using two angles $\vartheta_r^a(\vartheta_t^a)$ and $\varphi_r^a(\varphi_t^a)$ giving anomalous reflection and refraction, respectively (reprinted with permission from [97], © 2012 American Chemical Society). (c, d) SEM image ((c) top view; (d) side view) of fabricated metalens (diameter = 300 μm; focal length = 200 μm). (e, f) Measured focal spots and FWHMs of the metalenses at operational wavelengths of 405 nm; FWHM = 385 nm; NA = 0.6 (reprinted with permission from [98], © 2016 American Chemical Society). (g) Design of flat lens: intensity profiles for focal region and transverse cross-section of lens and axicon (reprinted with permission from [97], copyright © 2012 American Chemical Society). (h) A multifoci lens illuminated by an infinitely parallel (LP = LCP + RCP) light at $\theta = 0°$. Three focal planes are highlighted as $F1$, $F2$, and $F3$, respectively, with theoretical intensity profiles of the light behind the metalens in y-z plane at a wavelength of 740 nm. (i) Decrease in focal length with an increase in focal depth (source: Chen et al. [40], licensed under Creative Commons CC). (j) Monolayer flat lens diffraction-limited imaging using TMDC material (WSe_2 ; diameter = 300 μm; focal length = 300 μm) fabricated using femtosecond laser fabrication. (k) Microscopic image of the object "F" (l) second and (m) first order. (n) Microscopic image of the USAF standard board (o) second and (p) first order (source: Lin et al. [105], licensed under Creative Commons CC). (q) Nanowaveguide array for wavefront shaping (reprinted with permission from [24], copyright © 2014 American Chemical Society). (r–t) Superoscillatory lens of 40 μm diameter, with 100 radial rings. (s) Magnified view of super-oscillatory lens (t) Intensity of diffraction patterns obtained via simulation within propagation distance of 20 μm (source: Yuan et al. [109], licensed under the terms of the Creative Commons CC). (u) Nanoslit array in a metallic film forming a cylindrical lens with simulated intensity of diffraction patterns (source: Verslegers et al., reprinted with permission from [106], copyright © 2009 American Chemical Society).

frequency simple and advanced fabrication techniques such as single-step lithography and vertical integration have favored ultrathin, lightweight, and multifunctional flat lenses, along with features of diffraction-limited focusing and high-resolution qualities. Such sophisticated, portable, and compact designs, owing to their potential for vertical integration and adaptability, are capable of replacing their conventional voluminous counterparts by meeting the challenges and providing opportunities for applications like cell-phone camera modules, wearable displays, and bioimaging.

A flat lens is an assembly of optical antennas that are subwavelength-spaced scatterers engineered in a suitable size, shape, position, and orientation to scatter light with equal amplitude and cover phase over 0 to 2π range [97]. Many variants of metalens design including spin-selected, broadband, spin-insensitive, and polarization-controlled lenses have so far been presented. The efforts have continued to improve designs that are large in diameter, high in efficiency, and free from aberration to be used for sophisticated imaging. The intent to optimize the design parameters such as focusing efficiency, numerical aperture (NA), resolution, full-width half-maximum (FWHM), and Strehl ratio has resulted in a wide range of lens designs.

To have "high efficiency" lenses, a series of designs including multilayered metalens [69, 70] and all-dielectric metalenses [17, 71] have been proposed. A highly efficient, polarization-insensitive metalens composed of cylindrical nanopillars of a-Si:H ($n = 3.2475$) has exhibited an efficiency of 73.4% at the design wavelength of 633 nm. The authors in [98] have presented highly efficient, polarization-insensitive planar lenses on a glass substrate obeying the waveguiding effect for phase accumulation. The demonstrated lenses are TiO_2 nanopillars-based, have a diameter of 300 microns, NAs of 0.85 and 0.6 with respective highest efficiencies of 60% and 90% for red (660 nm), blue (532 nm), and green (405 nm) wavelengths. A symmetric diffraction-limited spot of 0.64λ has been recorded with high resolution, FWHM = $0.514\,\lambda$/NA and the Strehl ratios for horizontal cuts are 0.8, 0.82, and 0.83 for green, blue, and red wavelengths, respectively. Figures 3(c) and 3(d) show scanning electron microscope (SEM) images of the fabricated elements with nanopillars, while in Figures 3(e) and 3(f), the measured focal spots of the metalens at wavelengths of 405 nm and corresponding horizontal cuts of the focal spot are shown with FWHM of 385 nm.

In conventional optics, material dispersion leads to multiple foci, resulting in chromatic aberration, which is mitigated using multiple lenses for compensation of the difference of phase. In contrast, a design in [97], with hyperboloidal phase, produces spherical wavefront without paraxial bound and supports "aberration-less" focusing even at high NA. In the same way, to realize an aberration-free design, planar lenses and axicons consisting of a phased assembly of subwavelength-spaced optical nanoresonators have been demonstrated in [97] (Figure 3(g)). A diffraction-limited achromatic focusing for 470-670 nm is demonstrated using nanostructures of a thickness of the order of wavelength in [99]. Another wideband, highly efficient diffraction-limited achromatic metalens for wavelengths ranging from 1000 nm to 1700 nm is demonstrated with focusing efficiency of >64% in [100].

An important performance metric for metalenses is the size of the focus spot. The smaller the size, the better will be the resultant focus. A lens that is able to achieve the limiting focus spot size (λ/2NA) is said to exhibit diffraction-limited focusing at that wavelength. A single metalens made of an array of GaN nanoantennas has been reported to achieve diffraction-limited focusing with a subwavelength resolution for the entire visible spectrum [101]. A high-NA (0.97) metalens was demonstrated in [102], while NA > 1 has also been realized through immersion metalenses [103]. As another design variant, a 40 nm thick multifoci metasurface lens has been experimentally demonstrated in [40], which has three focal planes with CP keeping polarization states intact at the output as that of incident light (Figures 3(h) and 3(i)). Some of the recent research has attempted to test the validity of diffraction-limiting concepts by exploring opportunities for subdiffraction-limited focusing, as highlighted in [104]. Another important development in this domain has been the introduction of 2D materials, which have made flattening of lens design to atomically thin levels possible by virtue of their high refractive indices. In [105], a monolayer, ultrathin flat lens design method based on 2D materials using femtosecond laser writing is presented. This technique can induce local scattering inside the monolayer so as to aid in obtaining sufficient phase and amplitude modulation that has been a challenge for atomically thin 2D materials. The imaging with subwavelength resolution and diffraction limit for a range of magnifications and at different focal positions is achieved by the presented design (Figures 3(j)–3(p)).

Fresnel zone plates (FZPs) present yet another design variant for metalenses that function by diffraction-induced focusing of oblique incident light from half of the plate while blocking the other half using a binary mask, resulting in a gradual radial phase retardation. Nanoholes [24] (Figure 3(q)) and optical masks or nanoslits [106] at optical frequencies have been used for planar focusing. The phenomenon of superoscillation [107] is manifested when subdiffraction-limited [108] focusing occurs due to more frequent oscillations of band-limited functions as compared to the highest Fourier components. Longitudinal cross-sections of diffraction patterns and design of a superoscillatory lens have been shown in Figures 3(r)–3(t), which has a diameter of 40 microns [109], radially divided into 100 rings with a minimum annulus width of 200 nm. The lens' depth of focus and focal length were 4 μm and 10 μm, respectively. A flat lens consisting of rows of metallic slits that achieves focusing by nanopatterned gold films is shown in Figure 3(u) [106]. The simulated intensity of diffraction patterns for the design fabricated onto a 100 nm thick gold film layered on a glass substrate are shown within a propagation distance of 20 μm. For this design, the control of focusing behavior is a function of lens size and slit spacing. The applied design principle paves the way to engineer a wide range of optical components. In the past decade, extensive efforts have been made to achieve subdiffraction-limited resolution, where it was necessary either to place the lens in the

near-proximity of the object or fabricate on it [110]. In [111], a new microscope design for optical imaging with subdiffraction-limit is presented, surpassing the capabilities of conventional instruments and those of superlenses and hyperlenses. The proposed technique is so robust that it can be universally applied for an object placed thousands of nanometers away from the mask at any spectral wavelength, without depending on the lumens of the object itself and imposing no resolution limits.

The development of ultrathin metasurfaces has provided the means for greater control and better manipulation of angular momentum, amplitude, and phase, enabling the generation of special beams such as vortex, Bessel, and airy beams, which find applications in high-capacity data transmission, superresolution imaging, particle trapping, and the like.

An airy beam is a distinctive nondiffracting, self-accelerating waveform that traverses a curved trajectory in the forward direction [112]. The generation of a finite-energy airy beam at 633 nm with 73% amplitude of cross-component by engineering the amplitude and phase of transmitted EM wave has been presented in [113]. The amplitude profile of an airy beam can be defined by using

$$f(x) = \mathrm{Ai}(bx)\ \exp\ (ax) \tag{6}$$

where "a" is the positive value that keeps the beam's energy finite, "b" is transversal scale, "x" *is* the transverse coordinate, and "Ai" represents the airy function. Chen et al. have illustrated the shift in the direction of linearly polarized light by an all-dielectric, low-loss metasurface that imparts the desired phase and cross-polarized amplitude to incident light [112] [114] (Figures 4(a)–4(c)).

Bessel beams are Maxwell solutions of EM waves [115]. They form self-reconstructing, nondiffracting, and infinite-energy beams having transverse intensity and are described by Bessel function of the first kind. Bessel beam traversing in the z-direction is expressed in cylindrical coordinates as given by

$$E(r,\varnothing,z) = A.e^{ik_z z}.J_n(k_r r).e^{\pm \mathrm{in}\varnothing}, \tag{7}$$

where "A" is the amplitude, "k_z" and "k_r" are the corresponding lengthwise and axial wave vectors such that $k = 2\pi/\lambda$. In contrast to conventional axicons that are limited by an NA of 0.75 for generating 0^{th}-order Bessel beams, meta-axicons have not shown such limitations benefiting from more degrees of freedom in terms of compactness, design flexibility and features for the same purpose. Both plasmonics-based and all-dielectric meta-axicons have been exploited to generate zero- and higher-order Bessel beams in [44]. The study experimentally demonstrates that the all-dielectric, compact, and efficient meta-axicons platform, which is highly polarization-insensitive and has a high transmission efficiency of ~73.4%, is a winner in producing a multiorder Bessel beam for visible wavelength and with a propagation length of ~2600λ. In Figures 4(d)–4(f), the schematic description of two higher-order meta-axicons with different topological charges is shown [44]. A polarization-insensitive metasurface based on fully symmetric cascaded unit cells has also confirmed the generation of nondiffractive Bessel beams both numerically and experimentally [116]. They find plentiful applications in nanoparticle trapping [117], tractor beams [118], superresolution fluorescence imaging, light-sheet microscopy [119], optical bullets, and lithography and laser machining [120]. Bessel beams are suitable for high-power applications including high-resolution radar imaging, wireless charging [121], and microwave drilling [122].

Fractional-dimensional space Bessel beams (where the beam has an arbitrary noninteger dimension less than or equal to three) can model complex structures and have meritoriously enjoyed researchers' attention. A unique nondiffracting Bessel beam using fractional-dimensional space shown in Figures 4(g) and 4(h) is presented by Ehsan et al. in [123]. The technique can potentially encompass the limiting cases of both the ordinary integer and fractional Bessel beams. It is also capable of preserving the nondiffractive nature of Bessel and other structured light beams, along with being self-healing in nature, which refers to the restoring of amplitude downstream of an obstacle. Such beams provide a cutting-edge for light-based manipulation and trapping in near-field applications [123]. The wave equation $\nabla^2 E + \beta^2 E = 0$ is solved in fractional space where the Cartesian coordinates have fractional values such that $0 \le \alpha_1$, α_2, and $\alpha_3 \le 1$, where α_1, α_2, and α_3 are the spatial coordinates of fractional-dimensional space [124].

Light beams carry both linear [125] and angular momenta. The angular momentum can either be of spin (polarization-defined) or orbital (polarization-independent) types, as determined by the spatial distribution of light [83]. Spin angular momentum assumes only two values per photon ($\pm h$), whereas the orbital angular momentum (OAM) can assume multiple values as $l * h\ (l = 0,\pm 1,\pm 2,\cdots)$. A beam of light specified by its spatial distribution, having an annular intensity profile that projects itself as a spiral wavefront possessing a beam-axial phase singularity, i.e., a zero-intensity region [89, 126] and possessing OAM, is defined as a vortex beam (VB). Azimuthal phase gradients are responsible for helical wavefronts that generate VBs [127]. Beams with OAM have transformed many fields of modern-day photonics ranging from classical imaging to quantum communication systems. The wave having an OAM can provide an orthogonal degree of freedom to improve system capacity to hundreds of terabit per second (Tbps) for optical communication [128].

In conventional optics having larger footprints, many techniques including spiral phase plates (SPPs) [129], computer-generated holograms (CGHs) [130], fork grating [131], and cylindrical mode converters [132] have been deployed for OAM generation. In contrast, compact vortex beam generators have been developed by (i) downscaling conventional components, (ii) plasmonic vortex lenses [133], (iii) metasurfaces [134], (iv) integrated optical vortex emitters [135], and (v) subwavelength apertures and nanoslits. A compact, ultrathin, and miniaturized flexible plasmonic-based

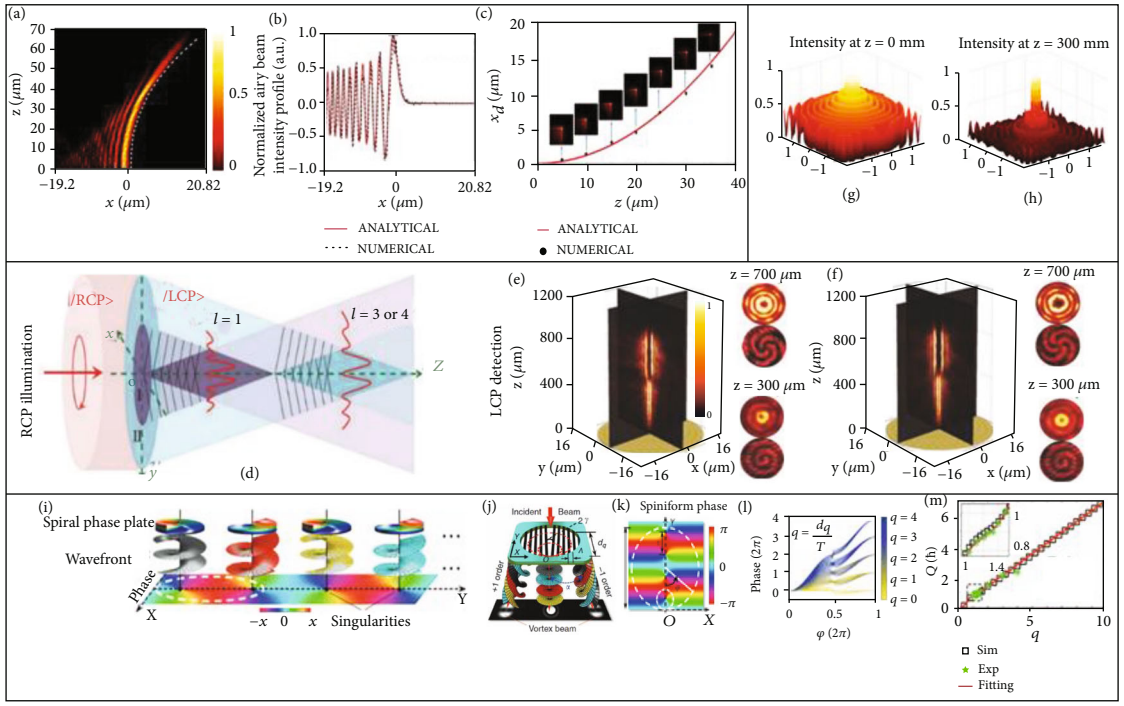

FIGURE 4: Light beams. (a–c) Airy beam. (a) Simulated E-field of 1D airy beam with dotted white curve representing bending trajectory of the main lobe. (b) Analytical and measured 1D airy beam intensity profiles. (c) 2D airy beam at different values of "z" ranging from 5 to 35 μm (Noureen et al. [114] © 2020, SPIE). (d–f) Cascaded Bessel beam generator. (d) Two-region helical axicons. Measured far-filed distribution of helical axicons and intensity profiles with interference patterns of beam (e) 1 and 3 and (f) 1 and 4 (source: Mei et al. [136], Copyright 2016, John Wiley and Sons). (g, h) Intensity profiles of space-fractional Bessel beams (s-SFBB) at (g) 0 mm and (h) 300 mm. α_1, α_2, and α_3 are set to 0.7, 0.9, and 1, respectively (source Ehsan et al. [124], copyright 2020, IEEE). (i–m) Analog vortex transmitter. (i) Helical wavefront of light with spatially separated phase singularities. (j) Schematic of the transmitter incorporating two periodic inclined gratings on a spiral aperture. (k) Vortex transmitter's phase profile: phase singularities are distanced by "τ", whereas the angle span is shown by ϕ between $\phi = 0$ and 2π. (l) Circumferential phase. (m) Average OAM of a photon as a function of diameter (figures adapted with permission from Ref. [36] © 2017, Light: Science & Applications).

device capable of complex light manipulation to produce OAM has been experimentally demonstrated in [136] using 121,000 rotated helical nanosieves.

After realization of integer, as well as fractional-order OAM, rational-order OAM had been a challenge, which was taken up in [36] using a bilaterally symmetrical grating metadevice creating an optical beam with dynamically varying spiniform-encoded phase over rational range. When light transits through "ℓ" perpendicularly oriented, concentric SPPs, its OAM of TC = 1 enhances [137]. As a proof-of-concept, it can be seen from Figures 4(i)–4(m) that as light passes through a series of transversely located SPPs, its OAM increases. The addition of light's OAM is proportional to the inclusion of SPPs because there are more phase singularities in the wavefront, thereby leading to the generation of continuous OAM through a gradually varying aperture [36].

An ultracompact array of nanowaveguides that converts light to a vortex beam is experimentally demonstrated in [24], such that it enables all-fiber structured light applications. Similarly, a flat logarithmic-spiral zone plate (LSZP) capable of breaking in-plane symmetry and hence providing enormous structural degrees of freedom has been presented in [138]. Optical vortices traverse crescent-shaped transverse intensity profiles with ~22% transmission efficiency and long focal depth in the broadband visible range, while the design in [139] traces light in a donut-like intensity. Analog OAM generation has also been realized using a single device, which benefits from linearly-varying transverse dislocation along symmetry axis [140]. The advancements in OAM-based designs catalyze researchers' interest to look for improved designs in terms of their signal-to-noise ratio (SNR). Therefore, in [141], a compact device with enhanced SNR and tunable multifocus VBs building multiple longitudinal vortices of different topological charges is presented.

The metalens design manifests a phase profile on the metasurface such that the waves that emerge out of the surface interfere constructively at the focal plane. A flat lens, in its simple configuration, follows a phase profile defined in Equation (8), whereas when merger of multiple phases takes place as given in Equation (10), the generation of "m^{th}-order" optical vortex beam, which is a superposition of Equations (8) and (9), is observed [142]. To realize the phase gradient in a dielectric-only metasurface, each nanoantenna positioned at (x_i, y_j) on the interface should ensure the required phase, given by the following equations:

$$\varphi_1\left(x_i, y_j\right) = \left[2\pi - \frac{2\pi}{\lambda_d} \times \left\{\sqrt{x_i^2 + y_j^2 + f^2} - f\right\}\right], \quad (8)$$

$$\varphi_2\left(x_i, y_j\right) = \left[\frac{m}{2}\right].\tan^{-1}\left(\frac{y_j}{x_i}\right), \quad (9)$$

$$\varphi_T\left(x_i, y_j\right) = \varphi_1\left(x_i, y_j\right) + \varphi_2\left(x_i, y_j\right), \quad (10)$$

where "f" represents the focal length, "m" is the topological charge equal to the number of interspersed helices at the focal plane, "x_i" and "y_j" specify the location of nano-antennas in the metasurface, and design wavelength is given by "λ_d" [141].

3.1. Metaholograms. Metaholography is another exciting field that counts on the manipulation of propagating EM waves. Holography is a real-world recording of an interference pattern resulting from diffraction in producing a light field that has complete information of the original scene. It is a lensless photography that carries the information of an object's amplitude and phase. Using metasurfaces, computer-generated holography (CGH) algorithms are employed that produce the required amplitude and phase profiles for a hologram [143]. CGHs require no object, which is an advantage over optical holography [144, 145]. If plasmonic materials are used in hologram designs, losses incur into the design [146]; hence, high refractive index nanostructures-based metasurfaces are employed [147]. Ansari et al. have proposed a dielectric-only, transmission-type metasurface, which employs a-Si:H having low absorption. The nanostructures utilized in the design of "helicity multiplexed" hologram are made up of a high-index dielectric. The demonstrated metahologram exploits the polarization control of nano-HWPs for visible wavelengths, which are optimized in terms of their geometry and sizes for realizing overlapping magnetic and electric dipoles in accordance with Huygen's principle [148].

In [39], polarization has been used as an extra degree of freedom and a visible domain metasurface with measured efficiency up to 61% possessing a much lower aspect ratio (≈ 4.7) has been presented, in comparison with the previously reported all-dielectric metasurfaces. The significant reduction in aspect ratio potentially eases out the fabrication complexities and cost requirements, making such CGHs an ideal candidate for their practical utility through large-scale production. The unit cell of the nanorod, along with its optical efficiency by varying orientation angle and wavelengths, is shown in Figures 5(a)–5(c). The proposed spin-controlled metahologram has performed better in terms of efficiency and image fidelities.

In [149], an ultrathin metasurface hologram with 30 nm thickness (~1/23rd of the operational wavelength) is experimentally demonstrated. The proposed design provides both amplitude and phase modulation and is capable of generating high-resolution low-noise images for visible wavelengths. In [23], another highly efficient, broadband, helicity multiplexed-type metahologram with a competitive image fidelity is presented. The hologram gives two distinct pieces of information as output for opposite helicity incident lights, which can be seen from Figures 5(d) and 5(e). In [15], a novel design with a 2D nanoarray of super-cells realizing a highly efficient, broadband, polarization-insensitive metahologram is presented. The hologram has been used to validate the polarization insensitivity of the proposed design numerically (Figure 5(f)), under illuminations from linear horizontal, linear vertical, left circular, and right circular polarization sources. The design has been characterized as a function of wavelength under unpolarized light incidence, where the efficiencies of 73%, 90% and 72% under the illumination of blue (488 nm), green (532 nm), and red (632 nm) lights, have been recorded respectively. The broadband nature of this design has been validated as its efficiency remains above 66% over the wavelength range (464 nm-650 nm) (Figure 5(g)). Similarly, a direction-multiplexed hologram has been demonstrated using a 2D array of all-dielectric super-cells to record different images in forward and backward directions. The proposed metahologram has been shown to provide a cost-effective solution with straightforward fabrication [30].

Conventionally, geometric holograms using spin-orbit-interactions (SOIs) exhibit only centrally symmetric images, thus limiting the capability of helicity multiplexing. As a possible solution, a spin-dependent, asymmetric metasurface is used to realize bidirectional propagation with high fidelity [150]. In [28], an asymmetric, SOIs-dependent, bidirectional, helicity-multiplexed metahologram for the visible domain has been presented for applications spanning from asymmetric data copying in communications to duplex displays in smart mobile devices. PB and retardation phases are exploited in such a way that two exclusive data items can be multiplexed into a single all-dielectric metasurface. The resulting metahologram showed ITU and POSTECH logos in accordance with the illumination direction from each side (Figures 5(h) and 5(i)).

Image holography means the realization of an image above the surface of the structure, i.e., without using a receiving screen. In [147], an image hologram is presented producing an image above the surface of the structure under arbitrary illumination like natural light. An image hologram for the target image "NANO" is produced using Si geometric metasurface by incorporating both geometric phase and magnetic resonance. The holographic image produced by the phase-only element is calculated using Kirchhoff's diffraction formula (Figure 5(j)). A high-fidelity reflection-based Fourier hologram has been designed for normally incident CP light that generates a wider image. The required phase mask is obtained using GS algorithm. The reflected light from silicon nanostructures that are quarter-wavelength thick projects a holographic image of a parrot (Figure 5(k)) in the far-field at the planes vertical to optical axis [147].

4. Applications of Metasurfaces

The compact and lightweight metasurface-based devices make next-generation system integration and device miniaturization possible. The characteristics of metamaterials to

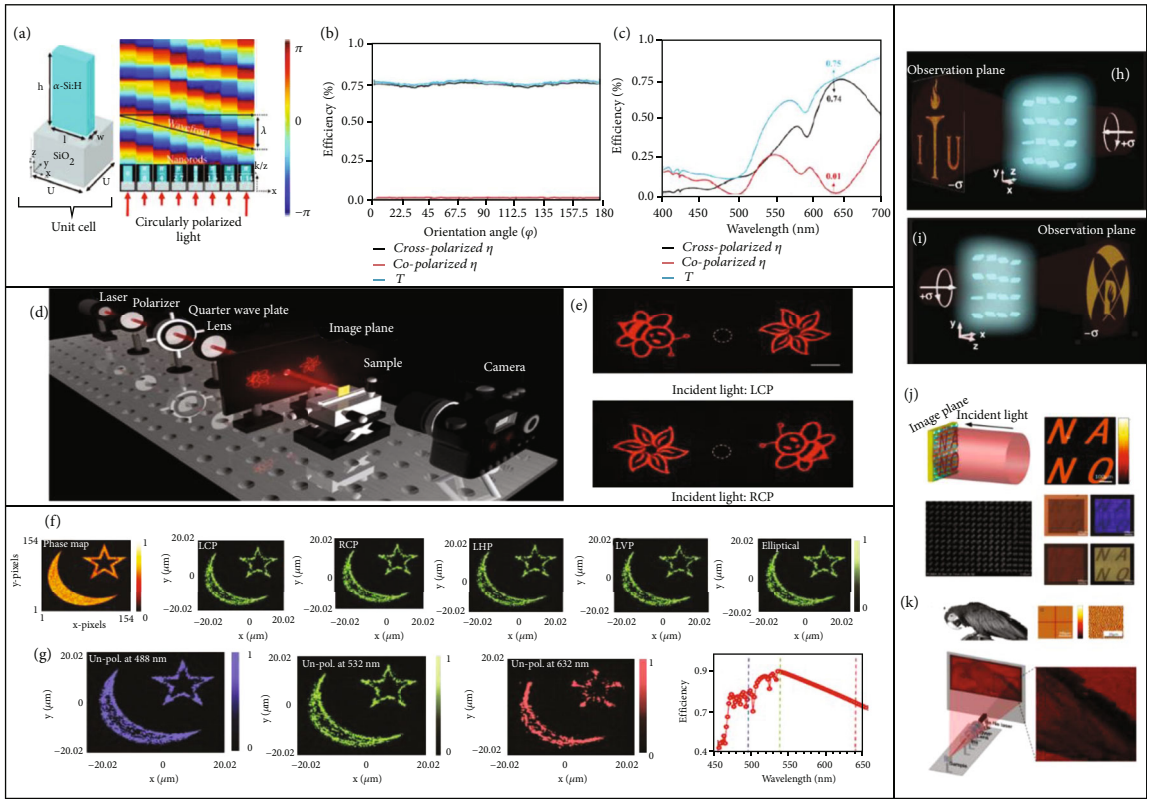

FIGURE 5: Metahalography. (a) Unit cell geometry of a single nanorod, with the wavefront obtained through full-wave simulation for complete 0-2π phase coverage. (b, c) Optical efficiencies with respect to (b) orientation angle (φ) of nanorods and (c) optical wavelengths for total, cross-, and copolarized transmissions, respectively, showing the maximum value of transmission and cross-polarized efficiencies (source: Ansari et al. [39] © 2019, John Wiley and Sons). (d, e) Reflective-type helicity multiplexed metasurface. (d) Optical characterization setup for measuring efficiencies and capturing high fidelity images of the fabricated samples. (e) Under LCP, 'flower' and 'bee' are on the left and the right side of incident beam , respectively while under RCP the information is swapped such that 'bee' and 'flower' are on the left and right sides of incident light, respectively (source: Wen et al. [23], licensed under the terms of the Creative Commons CC). (f, g) The polarisation-insensitive and broadband metahologram. (f) Reconstruction of holographic images at a wavelength of 532 nm under LCP, RCP, LHP, LVP, and elliptically polarized light with desired phase map of the target image (moon and star) (colored-orange). (g) Holographic image intensity profile under blue (488 nm), green (532 nm), and red (632 nm) unpolarized light illumination; the efficiency across the visible domain (450–650 nm) (source: Ansari et al. [15], copyright 2020 licensed under Copyright Clearance Center, Inc.). (h, i) Asymmetric wavefront generation. RCP light incident from (h) backward direction and (i) forward direction on an a-Si:H metasurface, showing complete utilization of an all-dielectric metasurface such that two independent pieces of information (ITU and POSTECH logos) (source: Naveed et al. [28], licensed under the terms of the Creative Commons CC). (j) A geometric metasurface-based hologram illustrating the working principle, phase accumulation for the word "NANO," and SEM image of fabricated meta-array with corresponding results. (k) A Fourier hologram with phase mask designed using Gerchberg-Saxton algorithm: a reflection-type hologram observed under CP using an experimental setup (reprinted with permission from [147], copyright © 2017 American Chemical Society).

furnish unusual material properties and achieve the desired light-matter interaction have fueled a lot of interest in the optical research community, leading to different applications and uses.

4.1. Solar Thermophotovoltaic (STPV) Systems. Sun is a perpetual and enormously huge source of energy that can be tapped for clean and renewable energy by employing PV cells. The traditional photovoltaics have limited efficiency in accordance with the Shockley-Queisser limit [151], because of broadband nature of the solar spectrum. The incident photon is either of low energy than the bandgap of the cell such that it is not absorbed, or of higher energy than the bandgap, causing thermal energy losses, allowing an upper efficiency limit of 33% without concentrating sun's spectrum and 41% with maximum achievable solar concentration [13] for single-junction PV cells. Solar thermophotovoltaics (STPVs) are an integration of a high-temperature, angle- and polarization-insensitive broadband absorber that absorbs the full spectrum of the sun and a spectral-selective emitter, which emits narrowband infrared radiation to PV cells, in order to couple solar radiation efficiently. They have been reported to exhibit a system efficiency as high as 85.4% [144]. However, laboratory demonstrations have so far been successful in achieving efficiencies not more than 35% due to associated inevitable energy losses [145].

Figure 6(c) shows a simplified diagram for an STPV system where the overall energy conversion process is decomposed into two parts.

4.2. Chirality. Chiral materials are meant to exhibit asymmetric behavior as chirality and asymmetric transmission go hand in hand [21]. Chirality indicates materials' inability to superimpose on their image, posturing a different material to incident EM wave from two different directions. Chirality, on most of the occasions, is artificially introduced by using metamaterials as natural materials do not exhibit high chirality. Chiral metamaterial helices have exhibited circular dichroism (CD) (absorption of a particular polarization). A 3D structure that reflects a certain CP light and absorbs the opposite handedness is presented by Mai et al. [152]. However, 3D chiral metamaterial helices employed for asymmetric transmission [153] cause increased difficulty in fabrication along with not being cost-effective, thereby needing 2D planar chiral metamaterials. Gansel et al. [153] proposed a highly efficient metamirror with CD enabling selective reflection with preserved handedness and complete absorption of other polarization. A multifunctional and fabrication-friendly design that exhibits full reflection for LCP without reversing its handedness and completely absorbing the other is presented in [154]. The proposed light-matter interaction example paves the path for detection and manipulation of CP light, encryption, and chiral imaging [153]. Wang et al. in [155] have elaborated metamirrors with CD for simultaneous spin-selective absorption and reflection using a multilayer structure. Since multilayer structures employed to achieve CD pose fabrication complexities, a unique single-layered all-dielectric metasurface for the visible regime is presented in [153]. Similarly, Jing et al. demonstrated a single-layer structure for selective absorption with maximum reflectance efficiency of ~58% by using different orientations and dimensions of the unit cell [156].

A distinctive chiroptical effect of simultaneous spin conservation and spin isolation using a novel design approach based on di-meta-atomic (a pair of achiral nanofins) platform is illustrated for optical frequencies (Figure 6(a)). The mutual coupling has resulted in both constructive and destructive interferences, thereby inducing a giant linear chiroptical effect in the form of CD, along with spin conservation, leading to the asymmetric transmission of 70% and average CD exceeding 60%, respectively. The design achieves 98% absorption of RCP and 72% reflectance for copolarized parameters of LCP, hence maximizing the performance through a single-layer metasurface [157]. There are possible applications of this phenomenon, such as chirality-dependent polarizers, sensors, spectroscopes, beam splitters, and polarization rotators and shapers [144]. Multipole scattering takes place in diatomic geometry. The compact, on-chip realization of giant chiroptical effects had long been a challenge at optical frequencies [144]. Naeem et al. in [145] have successfully achieved chiroptical effects by breaking the mirror and n-fold ($n = 2$) rotational symmetries. As much as 84% of cross-polarized light is reflected when RCP is illuminated and 80% is transmitted when LCP is impinged, thereby leading to 80% asymmetric transmission in reflection mode and 74% in transmission mode, verified using a hologram [145]. CD-based reflection structures have a specific application in optical setups that avoid bulkiness. Metamirrors without selective absorption for holographic applications [158] and vector beam generation at optical frequencies [159] have already been presented (Figure 6(b)).

4.3. Polarization Conversion. Polarization control of EM waves is a key issue in communication and imaging systems. Chiral anisotropic structures are capable of converting polarization, which is enabled by electric and magnetic coupling. A compact polarization converter is put forward in [160] for a subwavelength regime. Moreover, a bilayer meta-atom exhibiting high-efficiency transmission provides perfect polarization conversion of both orthogonal transmissions with an efficiency of 85%. The conversion efficiency is defined by

$$\eta_c = \frac{P_{\mp}}{P_{\mp} + P_{--}} \times 100\%. \tag{11}$$

The resulting efficiency values for transmission mode were reported as 59%, 58%, and 56% for "l" = 1, and 58%, 53.2%, and 48% for "l" = 2 at three distances, respectively [161].

4.4. Optical Tweezing. Particle trapping is another interesting area that has been extensively explored for improvements employing benefits associated with metasurfaces. Since 1970s, researchers have been on the lookout for ways to achieve the trapping of micrometer-sized particles. The success came with the concept of optical force used in the design of "optical tweezers" in subnanometers and microscales. Optical force is calculated in accordance with Lorentz law as there are two forces acting on the nanoparticle, i.e., gradient force and scattering force. Gradient force acts along the vertical and horizontal directions and should be greater when a particle is trapped, as against scattering force acting along propagation axis (z-axis). An optical tweezer that traps nanoparticles in the visible regime is presented numerically in [162], where the optical force was calculated on a 100 nm radius gold nanosphere. The particle was located at the focus of this metalens, resulting in a force of 30.8 pN, 24.7 pN, and 21.0 pN in the directions of three principal axes, respectively. The visible light trapping and the ease of manufacturing associated with these metadevices have made it possible to use them in many commercial optical gadgets requiring high-resolution imaging. Additionally, tweezers are employed to cool atoms and subatomic particles, and those in the micrometer range are used in microbiological research settings because of the transfer of momentum due to scattering of light [36].

4.5. Refractive Index Sensing. The refractive index is a constitutive parameter of a material that characterizes its EM response. Conventionally, differernt methods including photonic crystals [163], ring resonator sensors, and optical fiber systems [164] were used for measuring refractive index.

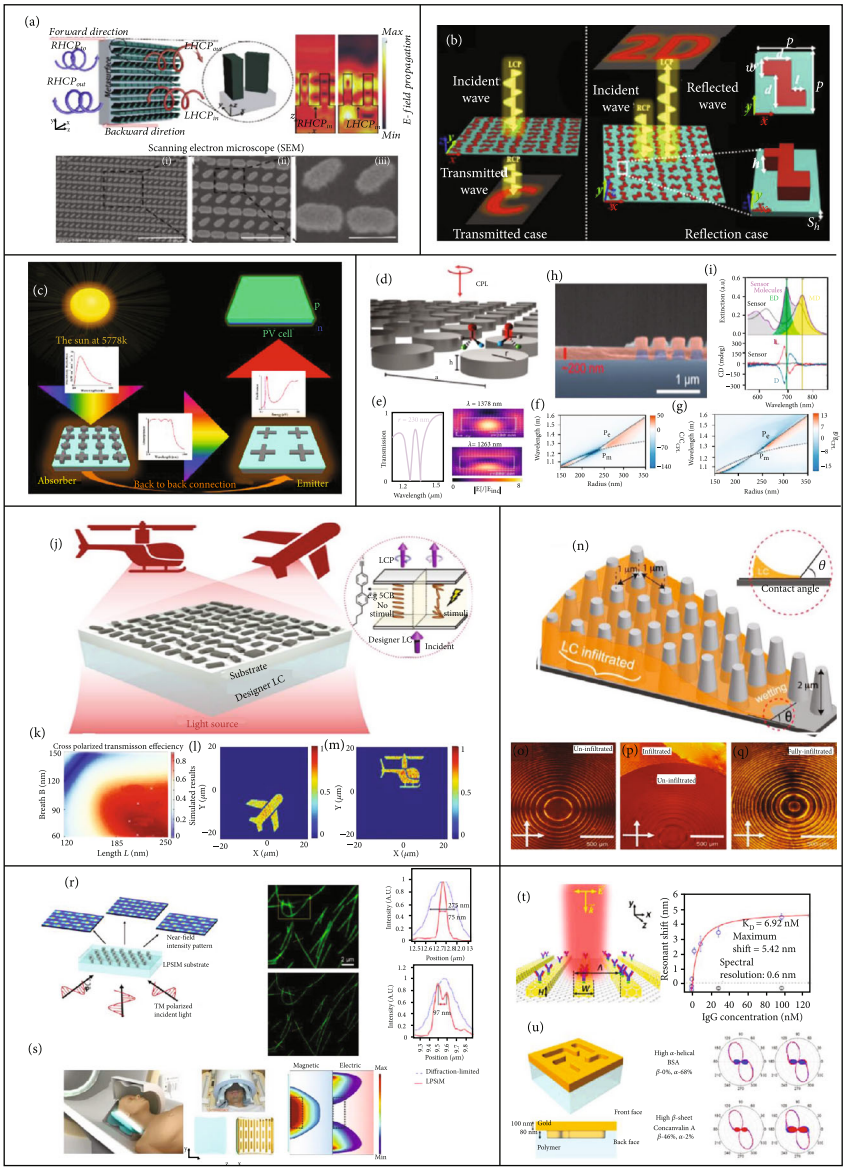

Figure 6: Metasurfaces in the real world. (a) Working principle and SEM images showing giant chirooptical effect in the visible regime (reprinted with permission from [144] © 2021 Photonics Research). (b) Illustration of the working principle to produce chiroptical effect in different modes (reprinted with permission from [145] © The Optical Society). (c) Schematic of an STPV system. Sunlight is given to an optical concentrator (broadband absorber+selective emitter), and the result is passed on to the cell for optimum solar energy utilization (source: Sarwar et al. [13] © 2021, licensed under the Creative Common). (d–g) Chirality exploiting refractive index sensing. (d) A chiral metasurface design. (e) Field enhancement using transmission information. (f) Optically enriched chirality. (g) Improved Kuhn's dissymmetry. (h, i) A dielectric resonator as chiral sensor (h) The fabricated device. (i) Measured CD represented (reproduced with permission from Joohoon Kim et al. Springer Nature [14] © 2021, licensed under Creative Commons). (j–m) Schematic illustration of a dynamic LC-integrated metasurface. (j) Polarization changes of light emitted from LC as a response to stimuli (left) and configuration changes of LCs with incoming stimuli and emission of LCP or RCP (right). (k) Contour map showing numerical optimization for high cross-transmission efficiency by varying length (L) and breadth (B) of 380 nm high metasurface. Simulated results of reconstructed hologram for (l) LCP incidence and (m) RCP incidence (source: Kim et al. [169], copyright © 2020, John Wiley and Sons). (n–q) Characterization of LC infiltration in the metalens system. (n) Illustration of LC infiltration into a regular SiO_2 nanopillars array of the metalens. The wetting layer is seen prior to full infiltration and the contact angle is measured at the edge of the infiltrated film droplet. (o–q) Optical analysis of meta-lens in cross-polarization during the infiltration process: (o) uninfiltrated, (p) partially infiltrated, and (q) fully infiltrated [173]. (r, s) Superresolution imaging for biomedical applications. (r) TM light is incident to capture the near-field intensity; both diffraction-limited and upper-resolution imaging are realized, depicted using green microtubules; sharpening of FWHM for the diffraction-limited imaging versus superresolution imaging. (s) Brain MRI scan using a metasurface showing local redistribution of magnetic and electric fields. (t, u) Detection of biomarkers. (t) Biosensor with periodic silicon nanowires; shifting of resonance resulting from various concentrations of IgG antibody. (u) A chiral solid-inverse metasurface structure with protein detection polar plots (source: Zhang et al. [178] © 2021, licensed under the Creative Common).

Metamaterials have also shown promise in the field of refractive index (RI) sensing. A low-loss high-performance RI sensor composed of TiO_2 with three different shapes (cylindrical, square, and elliptical) is presented in [165]. The sensor achieves sharp resonance dips indicative of high sensitivity, i.e., high Q-factor for four liquids (ethanol, carbon tetrachloride, pentanol, and water) having refractive indices between 1.333 and 1.453. RI sensors find industrial applications in food processing, chemical and environmental monitoring, biological sensing, biomedical, and quality control [165]. A metasurface design where nanoresonators (supporting electric dipoles) are combined with a ring resonator (supporting magnetic dipole) has the potential to increase the sensitivity of local index change [32]. Chiral metasurfaces, having broken mirror symmetry and exhibiting different optical behaviors for left or right CP light, have also aided the field of optical sensing [14] (Figures 6(d)–6(i)).

4.6. Reflection. Transmissive metasurfaces are reflective when they are backed by an added ground plane but the efficiency remains low because of the losses associated with the ground plane. All-dielectric metasurfaces support not only transmission-based but also are useful for reflection-based applications, where plasmonic metasurfaces have performed well conventionally. Near-perfect all-dielectric reflectors with 99.7% efficiency surpass metallic resonators with 80% reflection. A polycrystalline silicon- (poly-Si-) based dielectric resonator for maximum cross-polarized reflection and phase coverage is presented in [32]. Moreover, metareflectarrays (reflective metasurfaces) find applications in the domain of polarization selectivity. They are also capable of polarization conversion of incident EM waves into their opposite handedness upon reflection [166].

4.7. Microscopic Metavehicle. Another very recent and interesting application of nanostructured dielectric metasurfaces is in imparting an arbitrary phase gradient on an incident wavefront [167], where optomechanical effects are utilized to construct optical metavehicles. Metavehicles are microscopic particles having the potential to traverse significant distances using low-power plane-wave illumination. Directed propulsion is achieved by elongating nanoantennas in a propulsion direction while they are steered through the variation of polarization of the incident light and their complex patterned movement is realized. An added advantage is their ability to self-correct their motion while acting as locomotives for microscopic cargo and unicellular organisms. They have been shown to transport other microscopic objects by lateral pushing [168].

4.8. Active/Tunable Metasurfaces. "Real-time", active, flat metasurfaces that are capable of exhibiting changes in their optical properties upon triggers have also been explored in order to exploit tunability. In [169], liquid crystals- (LCs-) integrated metaholograms for nanosized dynamic displays are illustrated, which respond differently to various external stimuli. LCs are optically nonlinear, birefringent, and anisotropic in nature, thereby facilitating polarization control on a recurrent basis. The stimuli are sent to the device in electric, thermal, or mechanical form [169]. Phase change materials (PCMs) including germanium-antimony-tellurium (GST) alloys [170] and vanadium dioxide (VO_2) [171], mechanical actuations by altering geometric parameters or exploiting microelectromechanical systems (MEMS), and chemical reactions have helped such novel realizations. The inclination-dependent LC properties such as dielectricity, viscosity, elasticity, and optical birefringence [172] have provided leverage for controlling optical characteristics. Such responsive LC materials have been employed in various fields including displays (electric field), electric papers (pressure), and biological and chemical sensors (bacteria, molecular binding). The simple geometry of LC-integrated metasurface systems, where LC film is confined between two glass substrates over which preprogrammed metasurfaces are attached, provides an arbitrary control of polarization state of outgoing light. Figures 6(j)–6(m) show how the external stimuli are sensed in the cell so that encoded polarization is produced. The simulation results for optimizing the cell are presented in Figure 6(k), where using a contour map, the selection of optimized length (L), and breath (B) is achieved for high cross-transmission efficiency. The achieved simulated results of reconstructed hologram for LCP and RCP incidences are presented in Figures 6(l) and 6(m), respectively. The device performance has been evaluated experimentally as well, with an overall metasurface height of 380 nm.

In continuation of the ongoing art of utilizing light refraction, Lininger et al. have pioneered a design of a meta-lens that is also reconfigurable [173]. They have done so by coupling infiltrate LCs between microscopic pillars to achieve bending control of light. Previously, lenses were either combined or physically moved to have multiple bending possibilities. The LC control has enabled dynamically reconfigurable structured light. Significant modification is observed in focusing after infiltration of different liquid crystals, owing to the change of RI in structure's vicinity. The metalens infiltration is done in progression from no infiltration to partial infiltration and then complete infiltration, progressing circumferentially throughout the structure, and the results are shown in Figures 6(n)–6(q) for uninfiltrated, partially infiltrated, and fully infiltrated scenarios.

In the domains of public health, environmental monitoring, and military sector, the detection of biological and chemical substances is specifically important. Substance detection and visual reporting implementation on miniaturized scale aid these practical utilities. Therefore, a compact sensor platform that rapidly responds to gases using LCs without any further complex instrumentation to integrate LCs and holographic metasurfaces is proposed in [174], with the purpose to readily sense the presence of volatile gas and exhibit an instant visual holographic alarm. The holographic metasurface gas sensor platform provides a safety signal indicating the presence/absence of a dangerous gas. The two pieces of information are embedded in light polarization states, i.e., RCP corresponds to a "safe signal" and LCP corresponds to a "dangerous signal."

In order to further harness the potential of such exquisite benefits of metasurfaces, tunability is indispensable as it

conserves space for ideal metadevices exhibiting various electromagnetic responses by integrating diverse functionalities. The authors in [175] have illustrated the electrooptic effect to attain tunability for resonance wavelength and focal length using a visible metadevice. The designed metasurface has diffractive optical elements of barium titanate ($BaTiO_3$) on indium titanium oxide- (ITO-) coated substrate serving as an electrode. The electrical tuning causes the RI of the material to vary. Three different choices of applying voltage have been explored, i.e., application of (i) same potential to each of the elements, (ii) same potential to elements in either a row or a column, and (iii) different potentials to each of the elements. The tunability is validated by characterizing the parameters including point spread function (PSF), FWHM, and imaging. The resonance shift to different wavelengths (488 nm, 532 nm, and 633 nm) in the visible regime has been achieved under biased voltages of -8.9 V, -16.7 V, and -33.6 V, respectively.

4.9. Metasurfaces for Biomedical Applications

4.9.1. Bioimaging. Metasurfaces, while having induced deep interest in the consumer optoelectronics sector, have inspired and empowered novel bioimaging and biosensing devices as well. The extensive space requirements coupled with below-par performance of conventional optics hinder their deployment in clinical environments for accurate diagnoses. For studying internal organs at the millimeter scale and even beyond, high-resolution imaging can benefit from the inclusion of meta-lenses, such as in OCT (Figure 6(r)). It finds useful presence in ophthalmological examination, head and neck cancers, heart-related diseases, and medical diagnosis of various dermatological conditions. OCT provides morphological information of the sample by detecting the changes in RI of diverse biological media. Magnetic resonance imaging (MRI) is another medical imaging technique relying on strong magnetic fields and radiowaves for neuroimaging. MRI scans are time-consuming procedures, thus making the patient uncomfortable. Metasurfaces have been explored to reduce scan times and enhance MRI quality. They can simultaneously control and redistribute the radiofrequency electromagnetic field, improving SNR greatly and sufficiently reducing the scanning time [176] (Figure 6(a)). Likewise, DNA typing has also been realized using metasurfaces. A tortuous array of elliptical metasurfaces that detects binding of molecules has been designed and presented in [177].

4.9.2. Biosensing. Besides imaging for clinical purposes, a swift, robust, and dependable means for sensing to be employed in studies related to bacteria and viruses is also the need of the hour. Conventional methods in this arena are both tedious and time-consuming, while the methods including polymerase chain reaction (PCR) and mass spectrophotometry, despite being quicker, are exceptionally complex and costly to be used for swift detection on a frequent basis. Biosensors formulated using plasmonic- and/or dielectric-based metasurfaces present a rapid way to detect various microorganisms and cancer cells. Gold nanorod antennas have been used on a graphene layer to function as a metasurface biosensor whose performance is evaluated by measuring the detection of antibody immunoglobulin G (IgG), which binds with a biomolecule named protein A/G [178] (Figure 6(t)). Metasurface biosensors are employed in cancer biomarker detection (Figure 6(u)) for breast, liver, and oral cancers. An optofluidic, silicon nanoposts-based metasurface biosensor has been developed for breast cancer biomarkers detection to detect breast cancer at an early stage [179].

5. Future Directions: Design of Metasurfaces Based on 2D Materials

In order to miniaturize an optical structure to the atomic extent, 2D and van der Waals materials have emerged in the world of nanophotonics. Their capability of manipulating light flow due to their strong inelastic interactions with light invokes researchers' interest in exploiting the unprecedented miniaturization of optoelectronic components. Ultrathin flat optics is potent in controlling light at the subwavelength scale in comparison with the existing conventional refractive optics. High RIs of 2D materials support achieving the atomically thin dimensions. However, attaining diffraction-limited focusing and superresolution imaging through these materials are challenging because of their thickness-limited spatial resolution. A universal method that transforms the 2D monolayer into ultraflat lenses is described in [105]. Femtosecond laser direct writing technique generates local scattering in monolayer, providing an alternative of phase and amplitude modulation that otherwise had been a challenge for atomically thin 2D materials. The proposed technique achieves highly efficient 3D focusing with diffraction-limited imaging with nanometer resolution. Additionally, variable magnification for different focal positions under diffraction-limit has been realized. The design has remarkably eased out downscaling of optical devices composed of 2D materials by introducing a novel approach for fabricating ultrathin devices [105].

A single-layered molybdenum disulfide (MoS_2) having a giant optical path length (OPL) helps engineer the phase fronts of optical beams. The authors in [180] have exploited this feature in materializing the idea of sheer compactness using a few layers of MoS_2 with a total thickness of less than 6.3 nm. The electrotunability of RI for layered MoS_2 enables its utilization in microlenses having programmable focal lengths and an ultrahigh accuracy phase shifters, which are impossible to realize by bulk solids. In [181], the design of rewritable optical devices including lenses, prisms, and metalenses has been discussed. Upon light-matter interaction, rewritability is realized in these materials due to polaritons generation, which accumulate light and enable matter detection. Their shapes and sizes are tweaked to achieve reconfigurability [181]. The presented lenses assume flat 2D shapes as compared to their 3D counterparts: semicircle instead of a semisphere, triangle instead of a prism, and a simple line instead of an optical fiber [182].

Miniaturization poses an acute challenge of adjusting numerous unit elements in a minuscule device with

nonregular arrangements. In [183], a hybrid approach is developed analytically such that the random sieves control the amplitude, phase, and polarization of visible light for high accuracy. The model is experimentally demonstrated with ultrahigh capacity of nanosized holes (>34000 in number) to manifest subdiffraction-limited focusing. Moreover, a highly efficient diffraction-limited hologram is presented, which, in addition, is free from twin images present in conventional holography. Likewise, a multilayered, MoS_2-based, atomically thin photon-sieve for high-quality optical devices supporting strong excitonic resonances at the band-nesting region of MoS_2 is demonstrated in [55]. The design employs optical wavefront engineering in order to accumulate phase in OPL and confines the electromagnetic resonances of nanomodes, resulting in high transmission. Additionally, it facilitates high-fidelity nanofabrication. The supercritical 2D lens is capable of breaking diffraction limit and exhibits aberration-less high-resolution imaging in air. The authors have also reported a 10 times improvement in efficiency in relation to 2D nanosieve hologram obtained using their design. Photonic platforms made out of TMDCs open up new opportunities for future 2D metaoptics and nanophotonics [55].

The utilization of 2D materials is not only limited to transmissive applications but also has been extended to absorptive devices. In [184], a tunable absorber with absorption in the visible region based on a MoS_2 monolayer is presented. The design of the absorber is such that MoS_2 is sandwiched between Ag and SiO_2. It offers absorption in optoelectronics applications and provides tunability with geometric and optical parameters.

6. Conclusion

Amplitude, phase, and polarization are three fundamental characteristics of light waves, which open avenues to explore them as degrees of freedom for various application manifestations. Information can be stored in either of them; thus, wavefront manipulation becomes realizable. Conventional optical elements having the capability to manipulate light including lenses, wave plates, polarizers, beam splitters, and reflectors are voluminous and thus get ruled out of being used in integrated photonic devices. To overcome such issues, metasurfaces have been the focus of attention in the fields of optics and photonics, primarily due to tunable intrinsic properties of permittivity and permeability. Earlier, most of the metasurface designs were plasmonic material-based raising serious challenges in terms of fabrication, cost, and high resistive losses. The ability of metasurfaces to manipulate the EM wavefront is more efficiently exploited using all-dielectric materials to mitigate the issues associated with metal-based metasurfaces for transmissive applications.

With the passage of time, various novel phenomena and design techniques for ultracompact metasurfaces have emerged and matured, offering a myriad of applications. Metasurfaces are found in almost every field of science including medicine, biology, optics and photonics, and security. Many sophisticated techniques including electron beam lithography, focused ion beam, interference lithography, nanoimprint lithography, and femtosecond laser writing exist to fabricate metasurfaces at nanoscale. Optical absorbers find utilization in applications covering the full range of EM spectrum, including but not limited to photodetectors, stealth technology, photovoltaic and photochemical cells, optical filters, thermal light sources, thermal imaging, and thermal camouflaging, while single-wavelength or narrowband absorbers find applications in color filtering with enhanced color purity. A variety of metalenses—spin-selected, broadband, spin-insensitive, and polarization-controlled—are employed in high-resolution medical imaging, defect detection, spectroscopy, endoscopy, full-color routing, robotic vision, self-driving vehicles, cellphone camera modules, and wearable displays. There exist possibilities to revolutionize various areas of present-day photonics, such as imaging and classical and quantum communication systems using light beams with OAM. The field of nanophotonics can benefit from chirooptical effects in terms of molecular sensing, biological and biochemical separation, advanced imaging, and precision spectroscopy. Optical tweezers are employed to cool atoms and subatomic particles, and those in the micrometer range are used in microbiological research. RI sensors developed using metasurfaces find industrial applications in chemical and environmental monitoring; biomedical, biological, and biochemical sensing; quality control; food processing; and the like. Light beams—airy, Bessel, and OAM—are beneficial in machining by laser, lithography, trapping of nanoparticles, and tractor beam microscopy. High-power applications like wireless charging, ultraresolution radar imaging, microwave drilling, and the creation of through-the-wall radar make use of Bessel beams. Active and tunable metasurfaces have also been proposed having the tendency to dynamically modulate the EM wave properties. Many methods such as electrical, mechanical, and thermal have been applied to metasurfaces for exploring tunability. The electrooptic effect has aided electrically tunable metadevices to exhibit multifunctional characteristics by varying the electrical input, thus making them useful for tunable integrated systems. Earlier, meta-atom design was solely dependent on computational electromagnetic methods like finite element methods, finite-difference time-domain method, method of moments, and transmission line matrix methods for studying their characteristics. Nowadays, efficient deep learning architectures are complementing conventional methods to speed up accurate design procedures. To further miniaturize the dimensions of structures, two-dimensional van der Waals materials are also being explored, with the result that atomically thin optical lenses measuring less than 6.3 nm in thickness have been fabricated, which consist of just a few films of MoS_2. In the world of flexible ultrathin and ultracompact devices, metasurfaces surely have a major role to play in shaping the future of light-matter interaction and its manipulation. It can be safely claimed that the research in this direction will progress further by digging deeper into relevant physical concepts and phenomena, in a bid to materialize more useful real-life applications.

Conflicts of Interest

The authors declare that there are no conflicts of interest.

Authors' Contributions

S. I, A. S. R, and Z. A has collectively written the manuscript, while M. Z, Y. M. and M. Q. M overall supervised the writing and polished it through various revisions.

Acknowledgments

The authors would like to acknowledge the research funding to the KAUST Innovative Technologies Labratories (ITL) from King Abdullah University for Science and Technology (KAUST).

References

[1] J. E. Spice, "The electromagnetic spectrum," in *Chemical Binding and Structure*, Pergamon, Turkey, 1964.

[2] M. Qasim Mehmood, J. Rho, and M. Zubair, "Electromagnetic wave manipulation with metamaterials and metasurfaces for future communication technologies," *Backscattering and RF Sensing for Future Wireless Communication*, pp. 179–203, 2021.

[3] M. Zubair, M. J. Mughal, and Q. A. Naqvi, *Electromagnetic Fields and Waves in Fractional Dimensional Space*, Springer Science & Business Media, 2012.

[4] D. R. Smith, W. J. Padilla, D. C. Vier, S. C. Nemat-Nasser, and S. Schultz, "Composite medium with simultaneously negative permeability and permittivity," *Physical Review Letters*, vol. 84, no. 18, pp. 4184–4187, 2000.

[5] A. N. Grigorenko, A. K. Geim, H. F. Gleeson et al., "Nanofabricated media with negative permeability at visible frequencies," *Nature*, vol. 438, no. 7066, pp. 335–338, 2005.

[6] R. W. Ziolkowski and E. Heyman, "Wave propagation in media having negative permittivity and permeability," *Physical Review E*, vol. 64, p. 15, 2001.

[7] G. V. Viktor, "The electrodynamics of substances with simultaneously negative values of ϵ and *M*," *Soviet Physics Uspekhi*, vol. 10, no. 4, pp. 509–514, 1968.

[8] Z. Szabó, "Closed form kramers–kronig relations to extract the refractive index of metamaterials," *IEEE Transactions on Microwave Theory and Techniques*, vol. 65, no. 4, pp. 1150–1159, 2017.

[9] H. C. Van de Hulst and V. Twersky, "Light scattering by small particles," *Physics Today*, vol. 10, no. 12, pp. 28–30, 1957.

[10] X. Wang, J. Ding, B. Zheng, S. An, G. Zhai, and H. Zhang, "Simultaneous realization of anomalous reflection and transmission at two frequencies using bi-functional metasurfaces," *Scientific Reports*, vol. 8, no. 1, 2018.

[11] N. Mahmood, I. Kim, M. Q. Mehmood et al., "Polarisation insensitive multifunctional metasurfaces based on all-dielectric nanowaveguides," *Nanoscale*, vol. 10, no. 38, pp. 18323–18330, 2018.

[12] Y. B. Zhang, H. Liu, H. Cheng, J. G. Tian, and S. Q. Chen, "Multidimensional manipulation of wave fields based on artificial microstructures," *Opto-Electronic Advances*, vol. 3, pp. 1–33, 2020.

[13] A. S. Rana, M. Zubair, A. Danner, and M. Q. Mehmood, "Revisiting tantalum based nanostructures for efficient harvesting of solar radiation in STPV systems," *Nano Energy*, vol. 80, article 105520, 2021.

[14] J. Kim, A. S. Rana, Y. Kim et al., "Chiroptical metasurfaces: Principles, classification, and applications," *Sensors*, vol. 21, 2021.

[15] M. A. Ansari, T. Tauqeer, M. Zubair, and M. Q. Mehmood, "Breaking polarisation-bandwidth trade-off in dielectric metasurface for unpolarised white light," *Nanophotonics*, vol. 9, no. 4, pp. 963–971, 2020.

[16] A. S. Rana, I. Kim, M. A. Ansari et al., "Planar achiral metasurfaces-induced anomalous chiroptical effect of optical spin isolation," *ACS Applied Materials & Interfaces*, vol. 12, no. 43, pp. 48899–48909, 2020.

[17] F. Zhang, M. Pu, X. Li et al., "All-dielectric metasurfaces for simultaneous giant circular asymmetric transmission and wavefront shaping based on asymmetric photonic spin–orbit interactions," *Advanced Functional Materials*, vol. 27, no. 47, 2017.

[18] N. Liu and H. Giessen, "Coupling effects in optical metamaterials," *Angewandte Chemie International Edition*, vol. 49, no. 51, pp. 9838–9852, 2010.

[19] S. Chang, X. Guo, and X. Ni, "Optical metasurfaces: progress and applications," *Annual Review of Materials Research*, vol. 48, no. 1, pp. 279–302, 2018.

[20] X. L. Ma, M. B. Pu, X. Li, Y. H. Guo, and X. G. Luo, "All-metallic wide-angle metasurfaces for multifunctional polarization manipulation," *Opto-Electronic Advances*, vol. 2, pp. 1–6, 2019.

[21] A. Zahid, H. S. Khaliq, M. Zubair, T. Tauqeer, and M. Q. Mehmood, "Asymmetric transmission through single-layered all-dielectric metasurface," in *2020 17th International Bhurban Conference on Applied Sciences and Technology (IBCAST)*, pp. 26–30, Islamabad, Pakistan, 2020.

[22] Y. Fan, N. H. Shen, F. Zhang et al., "Graphene plasmonics: a platform for 2D optics," *Advanced Optical Materials*, vol. 7, 2019.

[23] D. Wen, F. Yue, G. Li et al., "Helicity multiplexed broadband metasurface holograms," *Nature Communications*, vol. 6, no. 1, p. 8241, 2015.

[24] J. Sun, X. Wang, T. Xu, Z. A. Kudyshev, A. N. Cartwright, and N. M. Litchinitser, "Spinning light on the nanoscale," *Nano Letters*, vol. 14, no. 5, pp. 2726–2729, 2014.

[25] N. Yu, P. Genevet, M. A. Kats et al., "Light propagation with phase discontinuities: generalized laws of reflection and refraction," *Science*, vol. 334, no. 6054, pp. 333–337, 2011.

[26] H. Markovich, I. I. Shishkin, N. Hendler, and P. Ginzburg, "Optical manipulation along an optical axis with a polarization sensitive meta-lens," *Nano Letters*, vol. 18, no. 8, pp. 5024–5029, 2018.

[27] S. A. Jalil, Q. S. Ahmed, M. Akram et al., "Fabrication of high refractive index TiO2films using electron beam evaporator for all dielectric metasurfaces," *Materials Research Express*, vol. 5, no. 1, 2018.

[28] M. A. Naveed, M. A. Ansari, I. Kim et al., "Optical spin-symmetry breaking for high-efficiency directional helicity-multiplexed metaholograms," *Microsystems and Nanoengineering*, vol. 7, no. 1, p. 5, 2021.

[29] A. Arbabi and A. Faraon, "Fundamental limits of ultrathin metasurfaces," *Scientific Reports*, vol. 7, no. 1, 2017.

[30] M. A. Ansari, I. Kim, I. D. Rukhlenko et al., "Engineering spin and antiferromagnetic resonances to realize an efficient direction-multiplexed visible meta-hologram," *Nanoscale Horizons*, vol. 5, no. 1, pp. 57–64, 2020.

[31] D. Tzarouchis and A. Sihvola, "Light scattering by a dielectric sphere: perspectives on the Mie resonances," *Applied Sciences*, vol. 8, no. 2, p. 184, 2018.

[32] Y. Yang, I. I. Kravchenko, D. P. Briggs, and J. Valentine, "All-dielectric metasurface analogue of electromagnetically induced transparency," *Nature Communications*, vol. 5, no. 1, p. 5753, 2014.

[33] R. C. Devlin, M. Khorasaninejad, W. T. Chen, J. Oh, and F. Capasso, "Broadband high-efficiency dielectric metasurfaces for the visible spectrum," *Proceedings of the National Academy of Sciences of the United States of America*, vol. 113, no. 38, pp. 10473–10478, 2016.

[34] K. Mohammadreza, A. Antonio, K. Pritpal, and C. Federico, "Broadband and chiral binary dielectric meta-holograms," *Science Advances*, vol. 2, article e1501258, 2021.

[35] S. Wang, P. C. Wu, V. C. Su et al., "A broadband achromatic metalens in the visible," *Nature Nanotechnology*, vol. 13, no. 3, pp. 227–232, 2018.

[36] K. Huang, H. Liu, S. Restuccia et al., "Spiniform phase-encoded metagratings entangling arbitrary rational-order orbital angular momentum," *Light: Science & Applications*, vol. 7, no. 3, p. 17156, 2018.

[37] Y. Guo, S. Zhang, M. Pu et al., "Spin-decoupled metasurface for simultaneous detection of spin and orbital angular momenta via momentum transformation," *Light: Science & Applications*, vol. 10, no. 1, p. 63, 2021.

[38] E. Plum, V. A. Fedotov, and N. I. Zheludev, "Planar metamaterial with transmission and reflection that depend on the direction of incidence," *Applied Physics Letters*, vol. 94, no. 13, article 131901, 2009.

[39] M. A. Ansari, I. Kim, D. Lee et al., "A spin-encoded all-dielectric metahologram for visible light," *Laser & Photonics Reviews*, vol. 13, pp. 1–9, 2019.

[40] X. Chen, M. Chen, M. Q. Mehmood et al., "Longitudinal multifoci metalens for circularly polarized light," *Advanced Optical Materials*, vol. 3, no. 9, pp. 1201–1206, 2015.

[41] A. Arbabi, E. Arbabi, Y. Horie, S. M. Kamali, and A. Faraon, "Planar metasurface retroreflector," *Nature Photonics*, vol. 11, no. 7, pp. 415–420, 2017.

[42] H. Lee, Z. Liu, Y. Xiong, C. Sun, and X. Zhang, "Development of optical hyperlens for imaging below the diffraction limit," *Optics Express*, vol. 15, no. 24, pp. 15886–15891, 2007.

[43] Q. Jiang, B. Du, M. Jiang et al., "Ultrathin circular polarimeter based on chiral plasmonic metasurface and monolayer MoSe2," *Nanoscale*, vol. 12, no. 10, pp. 5906–5913, 2020.

[44] N. Mahmood, H. Jeong, I. Kim et al., "Twisted non-diffracting beams through all dielectric meta-axicons," *Nanoscale*, vol. 11, no. 43, pp. 20571–20578, 2019.

[45] F. Zhang, X. Xie, M. Pu et al., "Multistate switching of photonic angular momentum coupling in phase-change metadevices," *Advanced Materials*, vol. 32, no. 39, article 1908194, 2020.

[46] K. Karthik, D. Huigao, S. Hegde Ravi, C. W. Koh Samuel, N. Wei Jennifer, and K. W. Yang Joel, "Printing colour at the optical diffraction limit," *Nature Nanotechnology*, vol. 7, pp. 557–561, 2012.

[47] V. M. Shalaev, "Transforming light," *Science*, vol. 322, no. 5900, pp. 384–386, 2008.

[48] S. An, C. Fowler, B. Zheng et al., "A deep learning approach for objective-driven all-dielectric metasurface design," *ACS Photonics*, vol. 6, no. 12, pp. 3196–3207, 2019.

[49] C. C. Nadell, B. Huang, J. M. Malof, and W. J. Padilla, "Deep learning for accelerated all-dielectric metasurface design," *Optics Express*, vol. 27, no. 20, pp. 27523–27535, 2019.

[50] S. Noureen, M. Zubair, M. Ali, and M. Q. Mehmood, "Deep learning based hybrid sequence modeling for optical response retrieval in metasurfaces for STPV applications," *Optical Materials Express*, vol. 11, pp. 3178–3193, 2021.

[51] S. An, B. Zheng, H. Tang et al., "Multifunctional metasurface design with a generative adversarial network," *Advanced Optical Materials*, vol. 9, no. 5, article 2001433, 2021.

[52] V. M. Shalaev, W. Cai, U. Chettiar et al., "Negative index of refraction in optical metamaterials," *Optics Letters*, vol. 30, no. 24, p. 3356, 2005.

[53] C. Enkrich, F. Pérez-Willard, D. Gerthsen et al., "Focused-ion-beam nanofabrication of near-infrared magnetic metamaterials," *Advanced Materials*, vol. 17, no. 21, pp. 2547–2549, 2005.

[54] H. Schift and A. Kristensen, *Nanoimprint Lithography*, Springer Handbooks, 2017.

[55] Z. Wang, G. Yuan, M. Yang et al., "Exciton-enabled meta-optics in two-dimensional transition metal dichalcogenides," *Nano Letters*, vol. 20, no. 11, pp. 7964–7972, 2020.

[56] S. Pancharatnam, "Generalized theory of interference and its applications," *Proceedings of the Indian Academy of Sciences - Section A*, vol. 44, no. 6, pp. 398–417, 1956.

[57] P. Ginzburg, F. J. R. Fortuño, G. A. Wurtz et al., "Manipulating polarization of light with ultrathin epsilon-near-zero metamaterials," *Optics Express*, vol. 21, no. 12, pp. 14907–14917, 2013.

[58] N. Dahan, Y. Gorodetski, K. Frischwasser, V. Kleiner, and E. Hasman, "Geometric Doppler effect: Spin-split dispersion of thermal radiation," *Physical Review Letters*, vol. 105, no. 13, 2010.

[59] L. Huang, X. Chen, H. Mühlenbernd et al., "Dispersionless phase discontinuities for controlling light propagation," *Nano Letters*, vol. 12, no. 11, pp. 5750–5755, 2012.

[60] M. Khorasaninejad, W. T. Chen, R. C. Devlin, J. Oh, A. Y. Zhu, and F. Capasso, "Metalenses at visible wavelengths: diffraction-limited focusing and subwavelength resolution imaging," *Science*, vol. 352, no. 6290, pp. 1190–1194, 2016.

[61] R. W. Wood, "On a remarkable case of uneven distribution of light in a diffraction grating spectrum," *Proceedings of the Physical Society of London*, vol. 18, pp. 269–275, 1901.

[62] A. S. Rana, M. Q. Mehmood, H. Jeong, I. Kim, and J. Rho, "Tungsten-based ultrathin absorber for visible regime," *Scientific Reports*, vol. 8, pp. 2–9, 2018.

[63] Z. Liu, G. Liu, G. Fu, X. Liu, and Y. Wang, "Multi-band light perfect absorption by a metal layer-coupled dielectric metamaterial," *Optics Express*, vol. 24, no. 5, pp. 5020–5025, 2016.

[64] Y. Zhou, M. Luo, S. Shen, H. Zhang, D. Pu, and L. Chen, "Cost-effective near-perfect absorber at visible frequency based on homogenous meta-surface nickel with two-dimension cylinder array," *Optics Express*, vol. 26, no. 21, pp. 27482–27491, 2018.

[65] I. Kim, S. So, A. S. Rana, M. Q. Mehmood, and J. Rho, "Thermally robust ring-shaped chromium perfect absorber of visible light," *Nanophotonics*, vol. 7, no. 11, pp. 1827–1833, 2018.

[66] K. Zhang, R. Deng, L. Song, and T. Zhang, "Broadband near-infrared absorber based on all metallic metasurface," *Materials*, vol. 12, no. 21, p. 3568, 2019.

[67] W. Li, U. Guler, N. Kinsey et al., "Refractory plasmonics with titanium nitride: broadband metamaterial absorber," *Advanced Materials*, vol. 26, no. 47, pp. 7959–7965, 2014.

[68] S. Ijaz, A. S. Rana, Z. Ahmad, B. Rehman, M. Zubair, and M. Q. Mehmood, "Exploiting zirconium nitride for an efficient heat-resistant absorber and emitter pair for solar thermophotovoltaic systems," *Optics Express*, vol. 29, no. 20, pp. 31537–31548, 2021.

[69] Q. Zhao, J. Zhou, F. Zhang, and D. Lippens, "Mie resonance-based dielectric metamaterials," *Materials Today*, vol. 12, no. 12, pp. 60–69, 2009.

[70] S. Wu, Y. Gu, Y. Ye, H. Ye, and L. Chen, "Omnidirectional broadband metasurface absorber operating in visible to near-infrared regime," *Optics Express*, vol. 26, no. 17, pp. 21479–21489, 2018.

[71] W. Guo, Y. Liu, and T. Han, "Ultra-broadband infrared metasurface absorber," *Optics Express*, vol. 24, no. 18, pp. 20586–20592, 2016.

[72] N. I. Landy, S. Sajuyigbe, J. J. Mock, D. R. Smith, and W. J. Padilla, "Perfect metamaterial absorber," *Physical Review Letters*, vol. 100, no. 20, article 207402, 2008.

[73] A. Zubair, M. Zubair, A. Danner, and M. Q. Mehmood, "Engineering multimodal spectrum of Cayley tree fractal meta-resonator supercells for ultrabroadband terahertz light absorption," *Nanophotonics*, vol. 9, no. 3, pp. 633–644, 2020.

[74] J. Hendrickson, J. Guo, B. Zhang, W. Buchwald, and R. Soref, "Wideband perfect light absorber at midwave infrared using multiplexed metal structures," *Optics Letters*, vol. 37, no. 3, pp. 371–373, 2012.

[75] B. Zhang, Y. Zhao, Q. Hao et al., "Polarization-independent dual-band infrared perfect absorber based on a metal-dielectric-metal elliptical nanodisk array," *Optics Letters*, vol. 19, pp. 15221–15228, 2011.

[76] Q. Qian, T. Sun, Y. Yan, and C. Wang, "Large-area wide-incident-angle metasurface perfect absorber in total visible band based on coupled Mie resonances," *Advanced Optical Materials*, vol. 5, no. 13, article 1700064, 2017.

[77] F. Ding, J. Dai, Y. Chen, J. Zhu, Y. Jin, and S. I. Bozhevolnyi, "Broadband near-infrared metamaterial absorbers utilizing highly lossy metals," *Scientific Reports*, vol. 6, no. 1, 2016.

[78] H. Hulkkonen, A. Sah, and T. Niemi, "All-metal broadband optical absorbers based on block copolymer nanolithography," *ACS Applied Materials & Interfaces*, vol. 10, no. 49, pp. 42941–42947, 2018.

[79] Z. Li, S. Butun, and K. Aydin, "Ultranarrow band absorbers based on surface lattice resonances in nanostructured metal surfaces," *ACS Nano*, vol. 8, no. 8, pp. 8242–8248, 2014.

[80] P. Tassin, T. Koschny, M. Kafesaki, and C. M. Soukoulis, "A comparison of graphene, superconductors and metals as conductors for metamaterials and plasmonics," *Nature Photonics*, vol. 6, no. 4, pp. 259–264, 2012.

[81] S. Cao, W. Yu, T. Wang et al., "Two-dimensional subwavelength meta-nanopillar array for efficient visible light absorption," *Applied Physics Letters*, vol. 102, no. 16, article 161109, 2013.

[82] M. Iwanaga, "Perfect light absorbers made of tungsten-ceramic membranes," *Applied Sciences*, vol. 7, no. 5, p. 458, 2017.

[83] Y. Lin, Y. Cui, F. Ding et al., "Tungsten based anisotropic metamaterial as an ultra-broadband absorber," *Optical Materials Express*, vol. 7, pp. 606–617, 2017.

[84] D. Huo, J. Zhang, Y. Wang, C. Wang, H. Su, and H. Zhao, "Broadband perfect absorber based on tin-nanocone metasurface," *Nanomaterials*, vol. 8, no. 7, p. 485, 2018.

[85] C. Liang, Z. Yi, X. Chen et al., "Dual-band infrared perfect absorber based on a Ag-dielectric-Ag multilayer films with nanoring grooves arrays," *Plasmonics*, vol. 15, no. 1, pp. 93–100, 2020.

[86] A. A. Shah and M. C. Gupta, "Spectral selective surfaces for concentrated solar power receivers by laser sintering of tungsten micro and nano particles," *Solar Energy Materials and Solar Cells*, vol. 117, pp. 489–493, 2013.

[87] A. S. Rana, M. Zubair, M. S. Anwar, M. Saleem, and M. Q. Mehmood, "Engineering the absorption spectra of thin film multilayer absorbers for enhanced color purity in CMY color filters," *Optical Materials Express*, vol. 10, no. 2, p. 268, 2020.

[88] V. Vashistha, G. Vaidya, R. S. Hegde, A. E. Serebryannikov, N. Bonod, and M. Krawczyk, "All-dielectric metasurfaces based on cross-shaped resonators for color pixels with extended gamut," *ACS Photonics*, vol. 4, no. 5, pp. 1076–1082, 2017.

[89] F. Cheng, J. Gao, S. T. Luk, and X. Yang, "Structural color printing based on plasmonic metasurfaces of perfect light absorption," *Scientific Reports*, vol. 5, no. 1, 2015.

[90] A. Raman, Z. Yu, and S. Fan, "Dielectric nanostructures for broadband light trapping in organic solar cells," *Optics Express*, vol. 19, no. 20, pp. 19015–19026, 2011.

[91] S. Wu, Y. Ye, Z. Jiang, T. Yang, and L. Chen, "Large-area, ultrathin metasurface exhibiting strong unpolarized ultra-broadband absorption," *Advanced Optical Materials*, vol. 7, pp. 1–7, 2019.

[92] C.-C. Chang, W. J. M. Kort-Kamp, J. Nogan et al., "High-temperature refractory metasurfaces for solar thermophotovoltaic energy harvesting," *Nano Letters*, vol. 18, no. 12, pp. 7665–7673, 2018.

[93] F. Aieta, M. A. Kats, F. Capasso et al., "Reflection and refraction of light from metasurfaces with phase discontinuities," *Journal of Biomedical Optics*, vol. 19, article 020901, 2014.

[94] X. Zhang, Z. Tian, W. Yue et al., "Broadband terahertz wave deflection based on C-shape complex metamaterials with phase discontinuities," *Advanced Materials*, vol. 25, no. 33, pp. 4567–4572, 2013.

[95] D. Hu, H. Wang, and Q. Zhu, "Design of six-band terahertz perfect absorber using a simple U-shaped closed-ring resonator," *IEEE Photonics Journal*, vol. 8, pp. 1–8, 2016.

[96] H. Zeng, Y. Zhang, F. Lan et al., "Terahertz dual-polarization beam splitter via an anisotropic matrix metasurface," *IEEE Transactions on Terahertz Science and Technology*, vol. 9, no. 5, pp. 491–497, 2019.

[97] F. Aieta, P. Genevet, N. Yu et al., "Out-of-plane reflection and refraction of light by anisotropic optical antenna metasurfaces with phase discontinuities," *Nano Letters*, vol. 12, no. 3, pp. 1702–1706, 2012.

[98] M. Khorasaninejad, A. Y. Zhu, C. Roques-Carmes et al., "Polarization-insensitive metalenses at visible wavelengths," *Nano Letters*, vol. 16, no. 11, pp. 7229–7234, 2016.

[99] W. T. Chen, A. Y. Zhu, V. Sanjeev et al., "A broadband achromatic metalens for focusing and imaging in the visible," *Nature Nanotechnology*, vol. 13, no. 3, pp. 220–226, 2018.

[100] Y. Wang, Q. Fan, and T. Xu, "Design of high efficiency achromatic metalens with large operation bandwidth using bilayer architecture," *Opto-Electronic Advances*, vol. 4, pp. 200007-200008, 2021.

[101] R. J. Lin, V.-C. Su, S. Wang et al., "Achromatic metalens array for full-colour light-field imaging," *Nature Nanotechnology*, vol. 14, no. 3, pp. 227–231, 2019.

[102] A. Arbabi, Y. Horie, A. J. Ball, M. Bagheri, and A. Faraon, "Subwavelength-thick lenses with high numerical apertures and large efficiency based on high-contrast transmitarrays," *Nature Communications*, vol. 6, no. 1, p. 7069, 2015.

[103] W. T. Chen, A. Y. Zhu, M. Khorasaninejad, Z. Shi, V. Sanjeev, and F. Capasso, "Immersion meta-lenses at visible wavelengths for nanoscale imaging," *Nano Letters*, vol. 17, no. 5, pp. 3188–3194, 2017.

[104] H. Yang, G. Li, X. Su et al., "Reflective metalens with sub-diffraction-limited and multifunctional focusing," *Scientific Reports*, vol. 7, no. 1, p. 12632, 2017.

[105] H. Lin, Z.-Q. Xu, G. Cao et al., "Diffraction-limited imaging with monolayer 2D material-based ultrathin flat lenses," *Light: Science & Applications*, vol. 9, no. 1, p. 137, 2020.

[106] L. Verslegers, P. B. Catrysse, Z. Yu et al., "Planar lenses based on nanoscale slit arrays in a metallic film," *Nano Letters*, vol. 9, no. 1, pp. 235–238, 2009.

[107] M. V. Berry and S. Popescu, "Evolution of quantum superoscillations and optical superresolution without evanescent waves," *Journal of Physics A: Mathematical and General*, vol. 39, no. 22, pp. 6965–6977, 2006.

[108] G. T. Di Francia, "Super-gain antennas and optical resolving power," *Nuovo Cimento*, vol. 9, no. S3, pp. 426–438, 1952.

[109] G. Yuan, E. T. F. Rogers, T. Roy, G. Adamo, Z. Shen, and N. I. Zheludev, "Planar super-oscillatory lens for sub-diffraction optical needles at violet wavelengths," *Scientific Reports*, vol. 4, p. 6333, 2014.

[110] X. Zhang and Z. Liu, "Superlenses to overcome the diffraction limit," *Nature Materials*, vol. 7, no. 6, pp. 435–441, 2008.

[111] E. T. F. Rogers, J. Lindberg, T. Roy et al., "A super-oscillatory lens optical microscope for subwavelength imaging," *Nature Materials*, vol. 11, no. 5, pp. 432–435, 2012.

[112] D. C. Chen, X. F. Zhu, Q. Wei, D. J. Wu, and X. J. Liu, "Broadband acoustic focusing by airy-like beams based on acoustic metasurfaces," *Journal of Applied Physics*, vol. 123, no. 4, article 044503, 2018.

[113] H. Ahmed, S. Noureen, N. Mahmood et al., "Highly efficient all-dielectric metasurfaces for airy beam generation in visible domain," in *2020 17th International Bhurban Conference on Applied Sciences and Technology (IBCAST)*, pp. 12–15, Islamabad, Pakistan, 2020.

[114] S. Noureen, H. Ahmed, N. Mahmood, M. Zubair, and M. Q. Mehmood, "Amplitude and Phase engineered all-dielectric metasurface for finite energy self-accelerating airy beam generation," *Nanoengineering: Fabrication, Properties, Optics, Thin Films, and Devices*, vol. 5, 2020.

[115] W. T. Chen, M. Khorasaninejad, A. Y. Zhu et al., "Generation of wavelength-independent subwavelength Bessel beams using metasurfaces," *Light: Science & Applications*, vol. 6, pp. e16259–e16259, 2017.

[116] M. R. Akram, M. Q. Mehmood, T. Tauqeer, A. S. Rana, I. D. Rukhlenko, and W. Zhu, "Highly efficient generation of Bessel beams with polarization insensitive metasurfaces," *Optics Express*, vol. 27, no. 7, pp. 9467–9480, 2019.

[117] G. Rui, X. Wang, and Y. Cui, "Manipulation of metallic nanoparticle with evanescent vortex Bessel beam," *Optics Express*, vol. 23, no. 20, pp. 25707–25716, 2015.

[118] A. Novitsky, C. W. Qiu, and H. Wang, "Single gradientless light beam drags particles as tractor beams," *Physical Review Letters*, vol. 107, no. 20, 2011.

[119] F. O. Fahrbach, P. Simon, and A. Rohrbach, "Microscopy with self-reconstructing beams," *Nature Photonics*, vol. 4, no. 11, pp. 780–785, 2010.

[120] M. Duocastella and C. B. Arnold, "Bessel and annular beams for materials processing," *Laser & Photonics Reviews*, vol. 6, no. 5, pp. 607–621, 2012.

[121] G. A. Landis, "Charging of devices by microwave power beaming," 2005, https://patents.google.com/patent/US6967462B1/en.

[122] S. Costanzo, G. Di Massa, A. Borgia, A. Raffo, T. W. Versloot, and L. Summerer, "Microwave Bessel beam launcher for high penetration planetary drilling operations," in *2016 10th European Conference on Antennas and Propagation (EuCAP)*, pp. 1–4, Davos, Switzerland, 2016.

[123] A. Ehsan, M. Q. Mehmood, Y. S. Ang, L. K. Ang, and M. Zubair, "Space-fractional bessel beams with self-healing and diffraction-free propagation characteristics," in *2020 14th European Conference on Antennas and Propagation (EuCAP)*, pp. 1–5, Copenhagen, Denmark, 2020.

[124] A. Ehsan, M. Q. Mehmood, K. Riaz, Y. S. Ang, and M. Zubair, "Unraveling the vector nature of generalized space-fractional Bessel beams," *Physical Review A*, vol. 104, no. 2, 2021.

[125] J. H. Poynting, "The wave motion of a revolving shaft, and a suggestion as to the angular momentum in a beam of circularly polarised light," *Orbital Angular Momentum*, vol. 3–9, 2016.

[126] M. Q. Mehmood, C.-W. Qiu, A. Danner, and J. Teng, "Generation of optical vortex beams by compact structures," *Journal of Molecular and Engineering Materials*, vol. 2, no. 2, article 1440013, 2014.

[127] Y. Liu and X. Zhang, "Metasurfaces for manipulating surface plasmons," *Applied Physics Letters*, vol. 103, no. 14, p. 141101, 2013.

[128] S. Mei, K. Huang, H. Liu et al., "On-chip discrimination of orbital angular momentum of light with plasmonic nanoslits," *Nanoscale*, vol. 8, no. 4, pp. 2227–2233, 2016.

[129] X. Chen, L. Huang, H. Mühlenbernd et al., "Dual-polarity plasmonic metalens for visible light," *Nature Communications*, vol. 3, no. 1, p. 1198, 2012.

[130] N. R. Heckenberg, R. McDuff, C. P. Smith, and A. G. White, "Generation of optical phase singularities by computer-generated holograms," *Optics Letters*, vol. 17, no. 3, p. 221, 1992.

[131] M. Padgett and L. Allen, "Light with a twist in its tail," *Contemporary Physics*, vol. 41, no. 5, pp. 275–285, 2000.

[132] M. W. Beijersbergen, L. Allen, H. E. L. O. van der Veen, and J. P. Woerdman, "Astigmatic laser mode converters and transfer of orbital angular momentum," *Optics Communications*, vol. 96, no. 1-3, pp. 123–132, 1993.

[133] H. Kim, J. Park, S.-W. Cho, S.-Y. Lee, M. Kang, and B. Lee, "Synthesis and dynamic switching of surface plasmon vortices with plasmonic vortex lens," *Nano Letters*, vol. 10, no. 2, pp. 529–536, 2010.

[134] P. Genevet, N. Yu, F. Aieta et al., "Ultra-thin plasmonic optical vortex plate based on phase discontinuities," *Applied Physics Letters*, vol. 100, no. 1, article 013101, 2012.

[135] N. K. Fontaine, C. R. Doerr, and L. L. Buhl, "Efficient multiplexing and demultiplexing of free-space orbital angular momentum using photonic integrated circuits," in *Optical Fiber Communication Conference*, pp. 1–3, Los Angeles, CA, USA, 2012.

[136] S. Mei, M. Q. Mehmood, S. Hussain et al., "Flat helical nanosieves," *Advanced Functional Materials*, vol. 26, no. 29, pp. 5255–5262, 2016.

[137] I. V. Basistiy, M. S. Soskin, and M. V. Vasnetsov, "Optical wavefront dislocations and their properties," *Optics Communications*, vol. 119, no. 5-6, pp. 604–612, 1995.

[138] H. Liu, M. Q. Mehmood, K. Huang et al., "Twisted focusing of optical vortices with broadband flat spiral zone plates," *Advanced Optical Materials*, vol. 2, no. 12, pp. 1193–1198, 2014.

[139] M. Q. Mehmood, H. Liu, K. Huang et al., "Broadband spin-controlled focusing via logarithmic-spiral nanoslits of varying width," *Laser & Photonics Reviews*, vol. 9, no. 6, pp. 674–681, 2015.

[140] K. Huang, H. Liu, M. Q. Mehmood et al., "Continuously shaping orbital angular momentum with an analog optical vortex transmitter," 2015, https://arxiv.org/abs/1504.01909.

[141] M. Q. Mehmood, S. Mei, S. Hussain et al., "Visible-frequency metasurface for structuring and spatially multiplexing optical vortices," *Advanced Materials*, vol. 28, no. 13, pp. 2533–2539, 2016.

[142] N. Mahmood, M. Q. Q. Mehmood, I. Lim et al., "Manipulating twisted light beam through all-dielectric metasurfaces," *High Contrast Metastructures*, vol. 37, 2019.

[143] C. Slinger, C. Cameron, and M. Stanley, "Computer-generated holography as a generic display technology," *Computer*, vol. 38, no. 8, pp. 46–53, 2005.

[144] H. S. Khaliq, I. Kim, A. Zahid et al., "Giant chiro-optical responses in multipolar-resonances-based single-layer dielectric metasurfaces," *Photonics Research*, vol. 9, no. 9, p. 1667, 2021.

[145] T. Naeem, A. S. Rana, M. Zubair, T. Tauqeer, and M. Q. Mehmood, "Breaking planar symmetries by a single layered metasurface for realizing unique on-chip chiroptical effects," *Optical Materials Express*, vol. 10, no. 12, p. 3342, 2020.

[146] K. Huang, Z. Dong, S. Mei et al., "Silicon multi-meta-holograms for the broadband visible light," *Laser & Photonics Reviews*, vol. 10, no. 3, pp. 500–509, 2016.

[147] Z. Li, I. Kim, L. Zhang et al., "Dielectric meta-holograms enabled with dual magnetic resonances in visible light," *ACS Nano*, vol. 11, no. 9, pp. 9382–9389, 2017.

[148] M. A. Ansari, M. Q. Mehmood, M. H. Waseem et al., "Helicity-multiplexed hologram via all-dielectric metasurface in the visible domain," in *2019 Conference on Lasers and Electro-Optics (CLEO)*, pp. 1-2, San Jose, CA, USA, 2019.

[149] X. Ni, A. V. Kildishev, and V. M. Shalaev, "Metasurface holograms for visible light," *Nature Communications*, vol. 4, no. 1, 2013.

[150] M. A. Naveed, M. A. Ansari, I. Kim et al., "A pragmatic metasurface with asymmetric spin interactions," in *CLEO: QELS_Fundamental Science*, Optical Society of America, 2020.

[151] W. Shockley and H. J. Queisser, "Detailed balance limit of efficiency ofp-nJunction solar cells," *Journal of Applied Physics*, vol. 32, no. 3, pp. 510–519, 1961.

[152] W. Mai, D. Zhu, Z. Gong et al., "Broadband transparent chiral mirrors: design methodology and bandwidth analysis," *AIP Advances*, vol. 9, no. 4, 2019.

[153] J. K. Gansel, M. Thiel, M. S. Rill et al., "Gold helix photonic metamaterial as broadband circular polarizer," *Science*, vol. 325, no. 5947, pp. 1513–1515, 2009.

[154] H. S. Khaliq, K. Riaz, M. Zubair et al., "Highly efficient metamirror with circular dichroism and wavefront engineering," *Metamaterials XII*, vol. 57, 2020.

[155] Z. Wang, H. Jia, K. Yao, W. Cai, H. Chen, and Y. Liu, "Circular dichroism metamirrors with near-perfect extinction," *ACS Photonics*, vol. 3, no. 11, pp. 2096–2101, 2016.

[156] L. Jing, Z. Wang, R. Maturi et al., "Gradient chiral metamirrors for spin-selective anomalous reflection," *Laser & Photonics Reviews*, vol. 11, no. 6, 2017.

[157] H. S. Khaliq, I. Kim, J. Kim et al., "Manifesting simultaneous optical spin conservation and spin isolation in diatomic metasurfaces," *Advanced Optical Materials*, vol. 9, no. 8, article 2002002, 2021.

[158] Y. Wang, C. Guan, X. Ding et al., "Multi-focus hologram utilizing Pancharatnam–Berry phase elements based metamirror," *Optics Letters*, vol. 44, no. 9, pp. 2189–2192, 2019.

[159] F. Ding, Y. Chen, Y. Yang, and S. I. Bozhevolnyi, "Multifunctional metamirrors for broadband focused vector-beam generation," *Advanced Optical Materials*, vol. 7, no. 22, p. 1900724, 2019.

[160] Z. Sun, B. Sima, J. Zhao, and Y. Feng, "Electromagnetic polarization conversion based on Huygens' metasurfaces with coupled electric and magnetic resonances," *Optics Express*, vol. 27, no. 8, pp. 11006–11017, 2019.

[161] M. R. Akram, M. Q. Mehmood, X. Bai, R. Jin, M. Premaratne, and W. Zhu, "High efficiency ultrathin transmissive metasurfaces," *Advanced Optical Materials*, vol. 7, no. 11, article 1801628, 2019.

[162] A. Ehsan, M. Zubair, T. Tauqeer, and M. Q. Mehmood, "Optical trapping of nanoparticles through artificially-engineered flat materials," in *2020 17th International Bhurban Conference on Applied Sciences and Technology (IBCAST)*, pp. 31–34, 2020.

[163] D. Yang, H. Tian, and Y. Ji, "High-Q and high-sensitivity width-modulated photonic crystal single nanobeam air-mode cavity for refractive index sensing," *Applied Optics*, vol. 54, no. 1, pp. 1–5, 2015.

[164] Q. Wu, Y. Semenova, P. Wang, and G. Farrell, "High sensitivity SMS fiber structure based refractometer – analysis and experiment," *Applied Optics*, vol. 19, no. 9, pp. 7937–7944, 2011.

[165] M. A. Abbas, A. Zubair, K. Riaz et al., "Engineering multimodal dielectric resonance of TiO_2 based nanostructures for high-performance refractive index sensing applications," *Opt. Express*, vol. 28, no. 16, pp. 23509–23522, 2020.

[166] H. S. Khaliq, M. R. Akram, K. Riaz et al., "Single-layered meta-reflectarray for polarization retention and spin-encrypted phase-encoding," *Optics Express*, vol. 29, no. 3, pp. 3230–3242, 2021.

[167] D. Fei, P. Anders, and I. B. Sergey, "Gradient metasurfaces: a review of fundamentals and applications," *Reports on Progress in Physics*, vol. 81, article 026401, 2018.

[168] D. Andrén, D. G. Baranov, S. Jones, G. Volpe, R. Verre, and M. Käll, "Microscopic metavehicles powered and steered by embedded optical metasurfaces," *Nature Nanotechnology*, vol. 16, no. 9, pp. 970–974, 2021.

[169] I. Kim, M. A. Ansari, M. Q. Mehmood et al., "Stimuli-responsive dynamic metaholographic displays with designer liquid

crystal modulators," *Advanced Materials*, vol. 32, no. 50, article 2004664, 2020.

[170] C. Choi, S. Y. Lee, S. E. Mun et al., "Metasurface with nanostructured Ge2Sb2Te5as a platform for broadband-operating wavefront switch," *Advanced Optical Materials*, vol. 7, no. 12, p. 1900171, 2019.

[171] F. Z. Shu, F. F. Yu, R. W. Peng et al., "Dynamic plasmonic color generation based on phase transition of vanadium dioxide," *Advanced Optical Materials*, vol. 6, no. 7, article 1700939, 2018.

[172] M. G. Clark, "The physics of liquid crystals," *Displays*, vol. 2, no. 3, p. 149, 1980.

[173] A. Lininger, A. Y. Zhu, J. S. Park et al., "Optical properties of metasurfaces infiltrated with liquid crystals," *Proceedings of the National Academy of Sciences of the United States of America*, vol. 117, no. 34, pp. 20390–20396, 2020.

[174] I. Kim, W. S. Kim, K. Kim et al., "Holographic metasurface gas sensors for instantaneous visual alarms," *Science Advances*, vol. 7, no. 15, 2021.

[175] T. Naeem, H. S. Khaliq, M. Zubair, T. Tauqeer, and M. Q. Mehmood, "Engineering tunability through electro-optic effects to manifest a multifunctional metadevice," *RSC Advances*, vol. 11, no. 22, pp. 13220–13228, 2021.

[176] A. P. Slobozhanyuk, A. N. Poddubny, A. J. E. Raaijmakers et al., "Enhancement of magnetic resonance imaging with metasurfaces," *Advanced Materials*, vol. 28, no. 9, pp. 1832–1838, 2016.

[177] A. Leitis, A. Tittl, M. Liu et al., "Angle-multiplexed all-dielectric metasurfaces for broadband molecular fingerprint retrieval," *Science Advances*, vol. 5, no. 5, p. eaaw2871, 2019.

[178] S. Zhang, C. L. Wong, S. Zeng et al., "Metasurfaces for biomedical applications: imaging and sensing from a nanophotonics perspective," in *Nanophotonics*, vol. 10, no. 1, pp. 259–293, 2021.

[179] Y. Wang, M. A. Ali, E. K. C. Chow, L. Dong, and M. Lu, "An optofluidic metasurface for lateral flow-through detection of breast cancer biomarker," *Biosensors and Bioelectronics*, vol. 107, pp. 224–229, 2018.

[180] J. Yang and Y. Lu, "Atomically thin optical lenses and gratings," in *Two–Dimensional Materials in Nanophotonics*, pp. 67–92, Jenny Stanford Publishing, 2019.

[181] A. Ambrosio, M. Tamagnone, K. Chaudhary et al., "Selective excitation and imaging of ultraslow phonon polaritons in thin hexagonal boron nitride crystals," *Light: Science & Applications*, vol. 7, no. 1, p. 27, 2018.

[182] K. Chaudhary, M. Tamagnone, M. Rezaee et al., "Engineering phonon polaritons in van der Waals heterostructures to enhance in-plane optical anisotropy," *Science Advances*, vol. 5, no. 4, 2019.

[183] K. Huang, H. Liu, F. J. Garcia-Vidal et al., "Ultrahigh-capacity non-periodic photon sieves operating in visible light," *Nature Communications*, vol. 6, no. 1, 2015.

[184] S. G. Zamharir, R. Karimzadeh, and X. Luo, "Tunable polarization-independent MoS2-based coherent perfect absorber within visible region," *Journal of Physics D: Applied Physics*, vol. 54, no. 16, article 165104, 2021.